Annual Report
Grant No. N00014-91-J-4164

(11)

September 15, 1991 - September 15, 1992

ENVIRONMENTALLY ASSISTED CRACKING OF HIGH STRENGTH BETA TITANIUM ALLOYS

Submitted to:

Dr. A. John Sedriks
Materials Division, Code 1131
Office of Naval Research
800 N. Quincy Street
Arlington, VA 22217-5000

Submitted by:

R. P. Gangloff
Professor

J. R. Scully
Assistant Professor

Graduate Students

L. M. Young
G. A. Young, Jr.
D. G. Kolman

SEAS Report No. UVA/525464/MSE93/101
October 1992

DEPARTMENT OF MATERIALS SCIENCE AND ENGINEERING

SCHOOL OF
ENGINEERING
& APPLIED SCIENCE

University of Virginia
Thornton Hall
Charlottesville, VA 22903

UNIVERSITY OF VIRGINIA
School of Engineering and Applied Science

The University of Virginia's School of Engineering and Applied Science has an undergraduate enrollment of approximately 1,500 students with a graduate enrollment of approximately 600. There are 160 faculty members, a majority of whom conduct research in addition to teaching.

Research is a vital part of the educational program and interests parallel academic specialties. These range from the classical engineering disciplines of Chemical, Civil, Electrical, and Mechanical and Aerospace to newer, more specialized fields of Applied Mechanics, Biomedical Engineering, Systems Engineering, Materials Science, Nuclear Engineering and Engineering Physics, Applied Mathematics and Computer Science. Within these disciplines there are well equipped laboratories for conducting highly specialized research. All departments offer the doctorate; Biomedical and Materials Science grant only graduate degrees. In addition, courses in the humanities are offered within the School.

The University of Virginia (which includes approximately 2,000 faculty and a total of full-time student enrollment of about 17,000), also offers professional degrees under the schools of Architecture, Law, Medicine, Nursing, Commerce, Business Administration, and Education. In addition, the College of Arts and Sciences houses departments of Mathematics, Physics, Chemistry and others relevant to the engineering research program. The School of Engineering and Applied Science is an integral part of this University community which provides opportunities for interdisciplinary work in pursuit of the basic goals of education, research, and public service.

Annual Report
Grant No. N00014-91-J-4164

September 15, 1991 - September 15, 1992

ENVIRONMENTALLY ASSISTED CRACKING OF HIGH STRENGTH BETA TITANIUM ALLOYS

Submitted to:

Dr. A. John Sedriks
Materials Division, Code 1131
Office of Naval Research
800 N. Quincy Street
Arlington, VA 22217-5000

Submitted by:

R. P. Gangloff
Professor

J. R. Scully
Assistant Professor

Graduate Students

L. M. Young
G. A. Young, Jr.
D. G. Kolman

Department of Materials Science and Engineering
UNIVERSITY OF VIRGINIA
SCHOOL OF ENGINEERING AND APPLIED SCIENCE
THORNTON HALL
CHARLOTTESVILLE, VA 22903-2442

SEAS Report No. UVA/525464/MSE93/101
October 1992

Copy No._____

REPORT DOCUMENTATION PAGE

Form Approved
OMB No. 0704-0188

1. AGENCY USE ONLY (Leave blank)	2. REPORT DATE	3. REPORT TYPE AND DATES COVERED
	October 1992	Annual 9-15-91 - 9-15-92

4. TITLE AND SUBTITLE
Environmentally Assisted Cracking of High Strength Beta Titanium Alloys

5. FUNDING NUMBERS
N00014-91-J-4164

6. AUTHOR(S)
J. R. Scully, R. P. Gangloff, L. M. Young, G. A. Young, Jr., D. G. Kolman

7. PERFORMING ORGANIZATION NAME(S) AND ADDRESS(ES)
University of Virginia
School of Engineering and Applied Science
Department of Materials Science and Engineering
Thornton Hall
Charlottesville, VA 22903-2442

8. PERFORMING ORGANIZATION REPORT NUMBER
UVA/525464/MSE93/101

9. SPONSORING/MONITORING AGENCY NAME(S) AND ADDRESS(ES)
Office of Naval Research
800 North Quincy Street
Arlington, VA 22217-5000

10. SPONSORING/MONITORING AGENCY REPORT NUMBER

11. SUPPLEMENTARY NOTES

12a. DISTRIBUTION/AVAILABILITY STATEMENT

12b. DISTRIBUTION CODE

13. ABSTRACT (Maximum 200 words)

The objective of this research is to define the conditions under which high strength β-titanium alloys are resistant to environmentally assisted cracking (EAC) in marine environments. Our goals are to: (1) characterize environment enhanced subcritical crack propagation behavior for metallurgical, chemical and mechanical loading conditions that could destabilize crack tip passive films to promote local dissolution and hydrogen uptake, (2) test the hydrogen embrittlement mechanism for EAC, and (3) develop a mechanism-based predictive model of EAC by integrating occluded crack chemistry, surface repassivation, hydrogen uptake and segregation at trap sites, and crack tip process zone micromechanics and damage. The behavior of two peak aged β alloys, Beta 21S (Ti-15Mo-2.7Nb-3Al by wt% and σ_{ys} = 1380 MPa) and Ti-15-3 (Ti-15V-3Cr-3Al-3Sn; σ_{ys} = 1315 MPa) plate, was emphasized during this reporting period. Three papers were published; each is summarized as follows.

14. SUBJECT TERMS	15. NUMBER OF PAGES
titanium alloys, hydrogen embrittlement, mechanical properties, intergranular cracking, transgranular cracking, microstructure, alpha precipitates, Beta phase, hydrides, passive film, Beta titanium alloys, fracture threshold	53
	16. PRICE CODE

17. SECURITY CLASSIFICATION OF REPORT	18. SECURITY CLASSIFICATION OF THIS PAGE	19. SECURITY CLASSIFICATION OF ABSTRACT	20. LIMITATION OF ABSTRACT
Unclassified	Unclassified	Unclassified	Unlimited

EAC resistance is characterized by a fracture mechanics resistance curve method that isolates crack propagation. Dynamic rising load tests with edge precracked specimens show that Beta 21S is susceptible to environmental cracking in aqueous 3.5% NaCl at -600 mV_{sce}. Relative to a moist air crack initiation toughness (K_{IC}) of 67 MPa$\sqrt{m}$, the threshold for stable crack growth (K_{th}) in chloride is as low as 38 MPa$\sqrt{m}$ and fracture occurs by intergranular separation. K_{th} is minimized at a crack tip strain rate of order 10^{-5} sec^{-1} or less, however, the existence of a sharp minimum is uncertain. While K_{IC} for Ti-15-3 is lower (K_{IC} = 58 MPa$\sqrt{m}$) than that of Beta 21S, cracking is unaffected by exposure to NaCl at several constant loading rates and intergranular cracking is not observed. EAC is not produced in Ti-15-3 or Beta 21S by either prolonged (24 hours) constant load exposure or high frequency low amplitude "ripple loading". Such loading is designed to rupture the crack surface passive film without inducing process zone volume fatigue damage. Methanol-NaCl-water solution may chemically destabilize crack surface passivity, but does not embrittle Ti-15-3 in conjunction with slowly rising load. EAC resistance differences between Beta 21S and Ti-15-3 are attributed to a higher yield strength and abundant α precipitation on β grain boundaries for the former alloy. Experiments, to be reported during Year 2 of this three year program, are in progress to: (a) define the relative importance of alloy strength and α precipitate microstructure, (b) characterize environmental fatigue crack propagation in each alloy, as related to monotonic load cracking, (c) establish the effect of applied electrode potential, and (d) define microscopic crack paths.

Hydrogen environment embrittlement is a possible mechanism for enhanced cracking in high strength β-titanium alloys. Notched tensile experiments, with varying hydrostatic constraint levels and electrochemically precharged hydrogen are employed to unambiguously distinguish the influence of hydrogen on fracture from that of aqueous dissolution, to establish the HEAC path, and to distinguish intrinsic effects of hydrogen from hydriding in the β-α microstructure. Rising load notched tensile tests are conducted at a strain rate similar to that causing the minimum K_{th} in NaCl solutions. Hydrogen concentrations ranging from as-processed levels (50 to 80 ppm) to 3400 ppm were investigated for peak aged Beta 21S. Neither hydriding of the β matrix nor subsurface α precipitates was detected by X-ray diffraction. However, a distinct increase in the lattice parameter of the BCC β matrix was observed at high hydrogen concentrations consistent with the partitioning of hydrogen to the β phase. Beta 21S is embrittled by dissolved hydrogen; crack nucleation and growth are progressively enhanced by higher levels of constraint and hydrogen concentration. These results suggest the existence of a critical tensile stress - internal hydrogen fracture criterion. A mixture of two transgranular fracture modes are also observed with increasing hydrogen concentration and constraint, cleavage-like and "interplate-transplate". A mixture of these modes as well as intergranular fracture is observed at the highest hydrogen concentrations and constraint levels. Intergranular separation is similar to that observed in aqueous environmental fracture tests, qualitatively confirming the role of hydrogen in the aqueous EAC case. Abundant α precipitation on β grain boundaries is suggested to have a detrimental role in HEAC since cleavage cracking is more typically observed for β alloys exposed to hydrogen and stress. Possible roles of grain boundary α include local stress induced hydriding, or strong hydrogen trapping and subsequent cracking at the α/β interface. Experiments in progress now include: (a) defining the exact role of grain boundary α from the hydrogen perspective, (b) completing hydrogen embrittlement studies for Ti-15-3 under the identical conditions for Beta 21S, and (c) determine the fracture initiation toughness (K_{IC}) of both Beta 21S and Ti-15-3 at various internal hydrogen concentrations using dynamic rising load tests.

Studies of the electrochemistry, passivity, and repassivation kinetics of ß titanium alloys have been undertaken to examine the relationships between microstructural-compositional factors and resulting crack tip chemistry, electrochemical dissolution kinetics, hydrogen production, and hydrogen absorption. Beta 21S, Ti-15-3, Grade 6 Ti (Ti-6Al-2.5Sn simulating α precipitates in peak aged ß-Ti), and commercially pure Ti do not exhibit major differences in passivity in neutral 3.5% NaCl, acidified 3.5% NaCl (pH = 1), 5M HCl, and a methanol-NaCl-water solution. All alloys exhibit a broad passive region under these conditions and no electrochemically active phases are detected for aged materials. Moreover, cathodic polarization studies indicate similar hydrogen evolution kinetics. Scratch repassivation experiments indicate similar bare surface open circuit potentials albeit well negative of the reversible electrode potential for the reduction of water indicative of high hydrogen fugacities. Similar repassivation rates were noted for each alloy. Auger electron spectroscopy with sputter depth profiling indicates a tendency to exclude oxidized Mo from the outer layers of the passive film for Beta 21S. In contrast a tendency exists for Cr oxidation in greater proportions than the concentration in Ti-15-3. However, for all alloys investigated a titanium rich oxide film is observed. The reduced EAC resistance of Beta 21S, compared to Ti-15-3, therefore can not be attributed to identifiable differences in the passivity or electrochemical properties of these alloys, at least in *simulated* crack chemistry solutions. Work in progress aims at (a) defining crack tip chemistries, (b) examining crack tip repassivation and hydrogen production rates under potential control in simulated crack environments, and (c) attempting to define hydrogen absorption under these conditions.

Future work will be aimed at development of a mechanism-based predictive model of EAC. This will be accomplished by proceeding in each of the specific areas indicated above. Additionally, other commercial high strength titanium alloys will be investigated.

To be published: Proceedings, Seventh World Conference on Titanium, S.H. Froes, ed., TMS-AIME, Warrendale, PA (1992).

HYDROGEN ENVIRONMENT EMBRITTLEMENT OF BETA TITANIUM ALLOYS

Lisa M. Young and Richard P. Gangloff

Department of Materials Science and Engineering
University of Virginia
Charlottesville, VA 22903-2442

Abstract

The hydrogen environment assisted cracking (HEAC) resistance of two peak aged metastable ß-titanium alloys, Beta 21S and Ti-15-3, is characterized by a fracture mechanics resistance-curve method. Rising load tests with aqueous 3.5% NaCl show that Beta 21S is susceptible to environmental cracking, presumably due to hydrogen embrittlement. Relative to a moist air crack initiation toughness (K_{IC}) of 67 MPa√m with transgranular fracture, the threshold for stable crack growth (K_{th}) in chloride is as low as 38 MPa√m and fracture occurs by intergranular separation. The magnitude of the reduction from K_{IC} to K_{th} depends on loading rate; for Beta 21S, K_{th} is minimized at intermediate crack tip strain rates of order 10^{-5} sec^{-1}.[1] In contrast the initiation toughness of Ti-15-3 in moist air is lower (58 MPa√m) than that of Beta 21S, but is unaffected by exposure to NaCl at several loading rates. HEAC is not produced in Ti-15-3 by either constant load exposure or by a high frequency low amplitude ripple load designed to rupture the crack surface passive film without inducing process zone volume fatigue damage. The poor HEAC resistance of Beta 21S, compared to Ti-15-3, is attributed to higher yield strength and abundant α precipitation on ß grain boundaries for the former alloy. The relative importance of each variable is not known.

Introduction

Metastable beta titanium alloys are being developed for marine, aerospace, petrochemical and medical implant applications that require formability, hardenability, high yield strength-fracture toughness and aqueous corrosion resistance [1-5]. The environmental cracking resistance of these alloys is of particular importance to long life, damage tolerant performance. Although the stress corrosion, hydrogen embrittlement and corrosion fatigue behaviors of α and α/ß-titanium alloys have been broadly characterized and modeled [6-8], the cracking resistance of ß-titanium alloys is relatively unexplored.

ß-titanium alloys are susceptible to brittle cracking in ambient temperature neutral aqueous environments with halide ions. Fracture mechanics experiments demonstrate that early developmental alloys (Ti-11.5Mo-6Zr-4.5Sn and Ti-13V-11Cr-3Al;

[1] *Strain rates in the original paper were in error and are corrected here.*

wt%) and binary model compositions (Ti-Mo), stressed in NaCl and KCl solutions, exhibit stable crack growth at stress intensities well below K_{IC} [7,9,10]. Fracture progresses by both intergranular separation and transgranular "cleavage" or "quasi-cleavage"; the cleavage plane is {100} [9]. Cracking is exacerbated at intermediate loading rates (crack tip strain rates) and applied electrochemical potentials (near -600 mV_{SCE}), and by increased yield strength (σ_{ys}) [7,10,11]. These trends were confirmed by experiments with smooth tensile specimens of a modern ß-titanium alloy, Ti-15V-3Cr-3Al-3Sn [12]. In contrast cathodic polarization is necessary for cracking in precracked specimens of Beta C (Ti-3Al-8V-6Cr-4Mo-4Zr) stressed in H_2S saturated acidified chloride solution [13].

It is reasonable to attribute cracking of ß-titanium alloys in aqueous electrolytes to hydrogen embrittlement (hydrogen environment assisted cracking, HEAC) because of the well known hydrogen susceptibility of high strength body-centered cubic steels, and because both gaseous hydrogen and cathodically precharged hydrogen embrittle ß-titanium alloys [14-16]. The HEAC mechanism for ß-titanium alloys in neutral chloride involves: (a) development of an occluded crack chemistry, (b) coupled crack surface dissolution, passive film formation and cathodic H production, (c) hydrogen absorption and diffusion into the crack tip process zone, (d) segregation at microstructural trap sites, and (e) hydrogen assisted microcracking, probably by decohesion, localized plasticity or hydride mechanisms. Passive crack surface films should play a central role in HEAC, with a sound passive film blocking hydrogen production and/or uptake. Variables; including alloy composition, microstructure, applied electrochemical potential, bulk electrolyte composition, microscopic slip deformation mode and dynamic cyclic strain; could compromise the passive film and enhance the uptake of embrittling hydrogen.

Research was initiated to investigate surface passivity and hydrogen production, uptake, trapping and embrittlement in the crack tip region of high strength ß-titanium alloys [17]. The objective of the work reported here is to characterize the environment assisted cracking behavior of two modern ß-titanium alloys, subjected to dynamic straining to destabilize crack tip passivity, and employing advanced fracture mechanics methods.

Experimental Procedure

Two alloys, Beta 21S (Ti-15Mo-2.7Nb-3Al-0.2Si-0.15 O; wt%) and Ti-15-3 (Ti-15V-3Cr-3Al-3Sn; wt%), were obtained as 10.2 and 9.5 mm thick hot rolled plate, respectively, in the solution treated conditions (871°C for 8 hours and 816°C for 30 minutes, respectively). Oversized blanks of each alloy were peak aged at 538°C for 8 hours. The resultant microstructures are homogeneous and isotropic in all directions, and consist of fine α platelets in a ß matrix of 100 μm diameter grains (Figs. 1 and 2). Each alloy is presumed to be stable with regard to ω and ß' precipitation. Future TEM studies will confirm this and define the morphology of the α precipitates [1-3,5,18]. Hardnesses for this aging condition are R_c 36.9 $\pm$ 1.3 for Ti-15-3 and R_c 42.5 $\pm$ 1.3 for Beta 21S. Based on the aging temperatures and measured hardnesses, the estimated tensile yield strengths of these alloys are 1025 MPa (Ti-15-3) and 1200 MPa (Beta 21S) [1,3].[2]

[2]Recent measurements establish that the yield strengths are in fact 1315 and 1380 MPa, respectively.

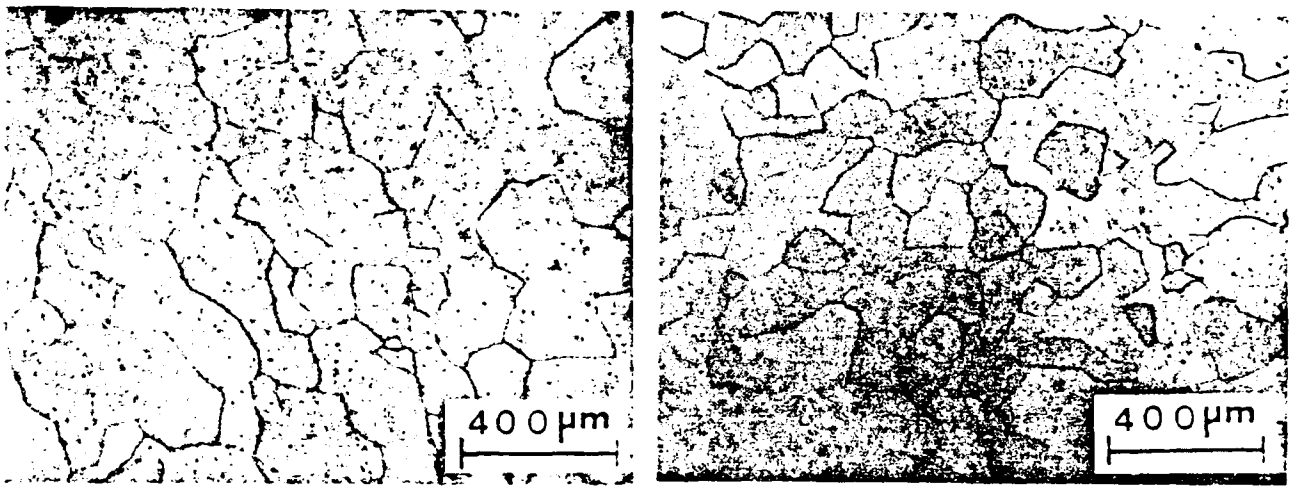

(a) (b)

Figure 1: Optical micrographs of as-received solution annealed ß-titanium alloys: (a) Beta 21S, (b) Ti-15-3.

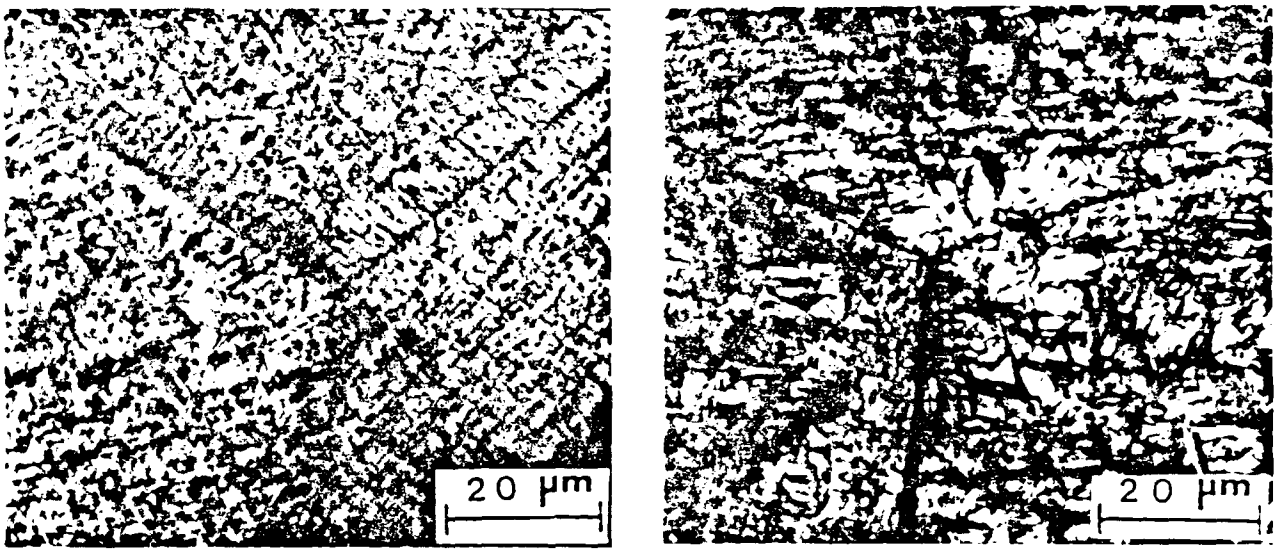

(a) (b)

Figure 2: Optical micrographs of peak aged alloys: (a) Beta 21S, (b) Ti-15-3.

HEAC resistance was characterized with a slowly rising load fracture mechanics method applied to fully rotating single edge precracked specimens (nominal crack length = 17.8 mm, thickness = 5.08 mm, width = 38.1 mm) [19-21]. A servohydraulic machine was employed for fatigue precracking (load control with K_{max} less than 30 MPa$\sqrt{m}$) and rising load cracking (actuator displacement control). Specimens were fatigue precracked in the aqueous environment, involving a three day exposure prior to the rising load experiment. Applied stress intensity (K) is calculated from measured load and crack length with a standard elastic solution [22]. Crack length is monitored using a computer-automated direct current (applied current = 2 to 4 amperes) potential drop (DCPD) method, including current polarity switching to eliminate thermal voltages and reference probes to account for temperature and current variations during prolonged experiments [23]. Data are presented as K versus crack extension increment (Δa). The threshold K for crack growth initiation is defined by the change in the slope of the initially linear electrical potential versus load record [24]. Environmental effects on crack propagation under increasing K are indicated by the slope of the K-Δa data. Small scale yielding is

maintained for all cases reported here. J-integral calculations indicate that J_{total} is approximated by $J_{elastic}$; thus elastic K analysis is sufficient. Crack initiation occurred under dominant plane strain constraint based on the J-integral approach (thickness > 25 $J_{initiation}/\sigma_{ys}$), however, the presence of shear lips indicated that the crack propagated under mixed plane stress and plane strain [19,20].

Fracture experiments were conducted in either moist air or 0.6M (3.5 wt%) NaCl at fixed electrode potential and 25°C. The central portion of the edge cracked specimen was immersed in flowing (60 ml/min) chloride (pH 8, 23°C) in a sealed plexiglass chamber. Environment control was complete; no dissimilar metal contacted the specimen, all tubing was teflon and the electrolyte was argon deaerated. The specimen was maintained at constant potential by a Wenking potentiostat in conjunction with a Ag/AgCl reference electrode and two platinum counter electrodes, each isolated to minimize solution contamination.

Results

Ti-15-3 is resistant to HEAC during rising load at various slow displacement rates; these conditions promote HEAC in ferritic and martensitic steels [15]. K-Δa results are presented in Fig. 3. The stress intensity at the initiation of crack growth (where Δa first is first nonzero) represents a threshold for HEAC (K_{th}), or an environment sensitive fracture toughness.

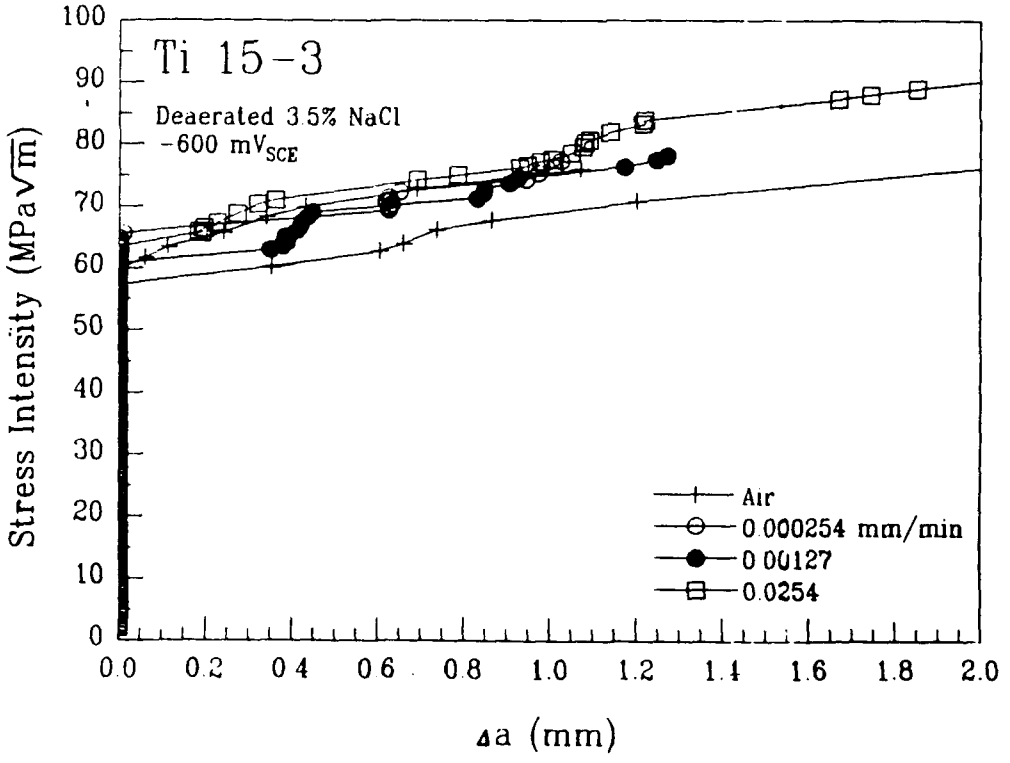

Figure 3: Rising load stress intensity versus crack extension data for Ti-15-3 in moist air and deaerated 3.5% NaCl (-600 mV_{sce}) as a function of loading rate.

For benign moist air, the initiation toughness (or K_{IC}) of Ti-15-3 is 57 and 59 MPa√m based on replicate experiments. For aqueous chloride at a fixed potential of -600 mV_{sce}, K_{th} ranges from 61 to 65 MPa√m, independent of actuator displacement rate varying between 0.025 and 0.00025 mm/min. The chloride environment does not

decrease the crack initiation toughness. For each environment, stable crack extension (finite $dK/d\Delta a$) is observed without an environmental influence. The difference in the slope of the K-Δa results is larger for the replicate air tests compared to the aqueous environmental effect; actuator displacement rate does not affect the HEAC propagation resistance of Ti-15-3. (The variability of the crack propagation results for moist air may be related to subtle inaccuracies in defining the electrical potential corresponding to crack initiation. The problem here is that crack tip plastic deformation, microvoid damage and macrocrack growth can contribute to voltage increases.) Crack growth bursts are noted for Ti-15-3 specimens at each displacement rate, but only for the aqueous environment. Discontinuous cracking was most apparent on the plot of crack length versus time. On the K-Δa plot, bursts are indicated by jumps in crack length between clustered data points.

Environment did not influence the microscopic fracture morphology for Ti-15-3. Typical scanning electron fractographs of the crack initiation region, adjacent to the fatigue precrack, are presented in Fig. 4 for the air and aqueous NaCl environments. For each case the crack surface is mainly populated by transgranular features indicative of microvoid-based cracking, as confirmed by high magnification observation, and perhaps associated with coarse α precipitates [27]. Scattered facets are present, indicating limited intergranular microvoid rupture or HEAC.

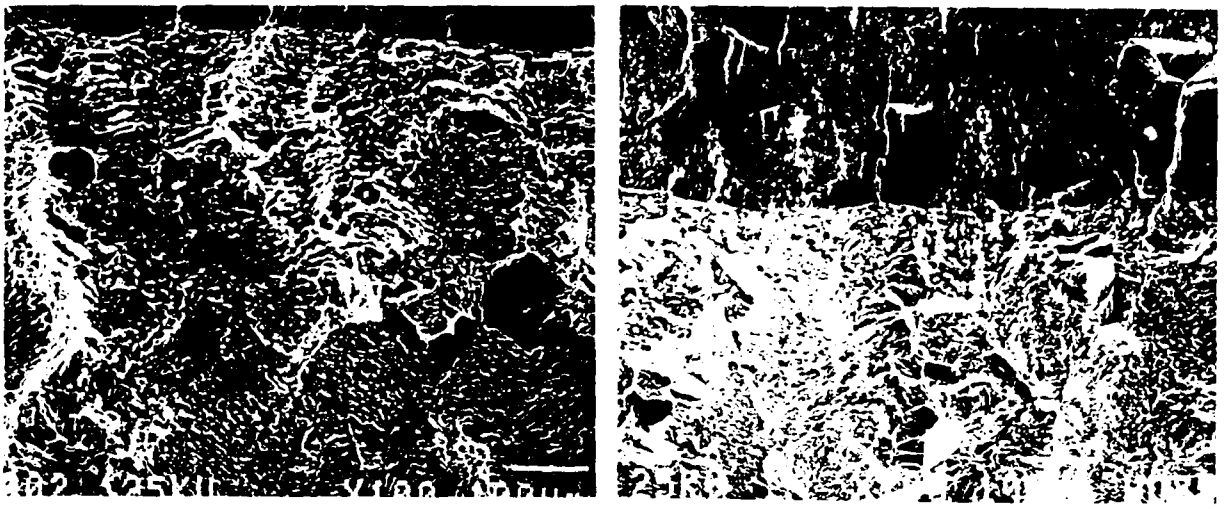

(a) (b)

Figure 4: SEM fractographs of the fatigue precrack (top) and rising load fracture toughness crack surfaces in Ti-15-3: (a) air; (b) deaerated 3.5% NaCl.

In contrast to Ti-15-3, Beta 21S is embrittled by aqueous chloride, as shown by the K-Δa data in Fig. 5. While K_{IC} is high (66 and 68 MPa$\sqrt{m}$) for moist air, K_{th} values range from 38 to 51 MPa$\sqrt{m}$ for Beta 21S in NaCl at -600 mV_{sce}. The macroscopic crack growth resistances (average $dK/d\Delta a$) are similar for each environment, however, crack bursts are observed for loading in NaCl. Limited experiments indicate that K_{th} values are increased if the specimen is fatigue precracked in moist air compared to the standard procedure of precracking in NaCl. For example, K_{th} equals 38 MPa$\sqrt{m}$ for precracking in NaCl and 58 MPa$\sqrt{m}$ for precracking in moist air, each at a constant actuator displacement rate of 0.0254 mm/min and in NaCl.

Actuator displacement rate affected HEAC of Beta 21S in NaCl. K_{th} is minimal at an intermediate loading rate (0.025 mm/min), with higher thresholds for crack

initiation at both faster and slower rates. Crack bursting in NaCl is observed for the two slowest loading rates.

Aqueous NaCl caused a dramatic fracture mode transition. The fractographs in Fig. 6 show that, while the air crack appears to involve intergranular microvoid fracture (with limited tear-free facets), the chloride case is almost entirely intergranular with little evidence of resolvable localized plasticity. This fracture mode transition is consistent with an environmental effect on fracture resistance.

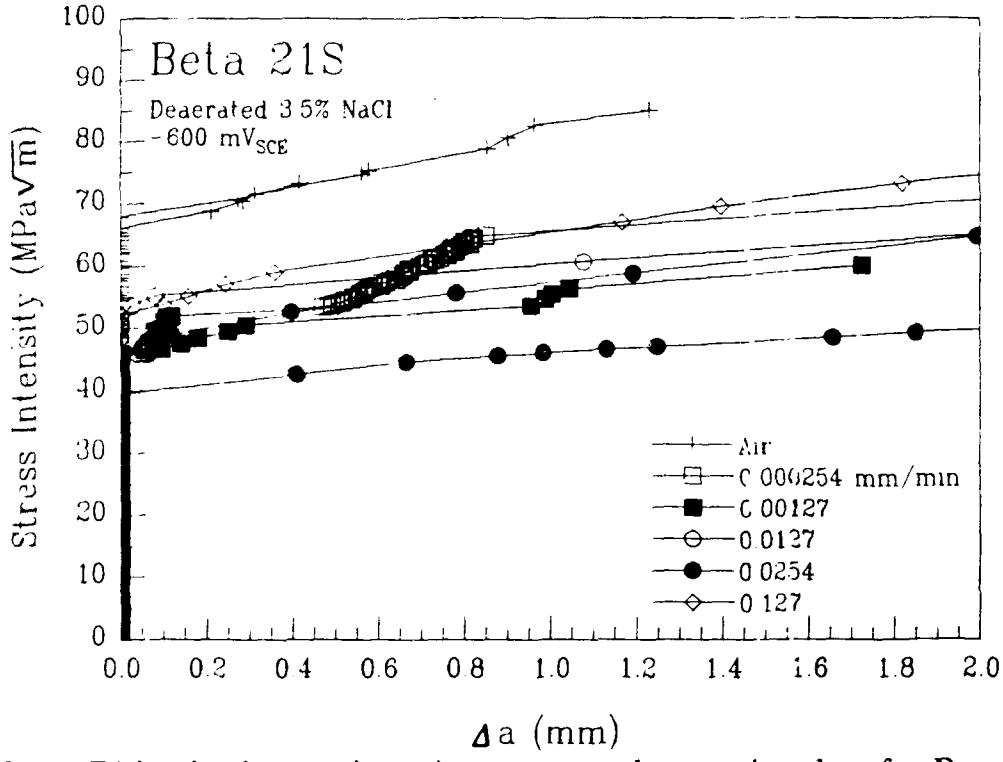

Figure 5. Rising load stress intensity versus crack extension data for Beta 21S in moist air and deaerated 3.5% NaCl (-600 mV_{sce}) as a function of loading rate.

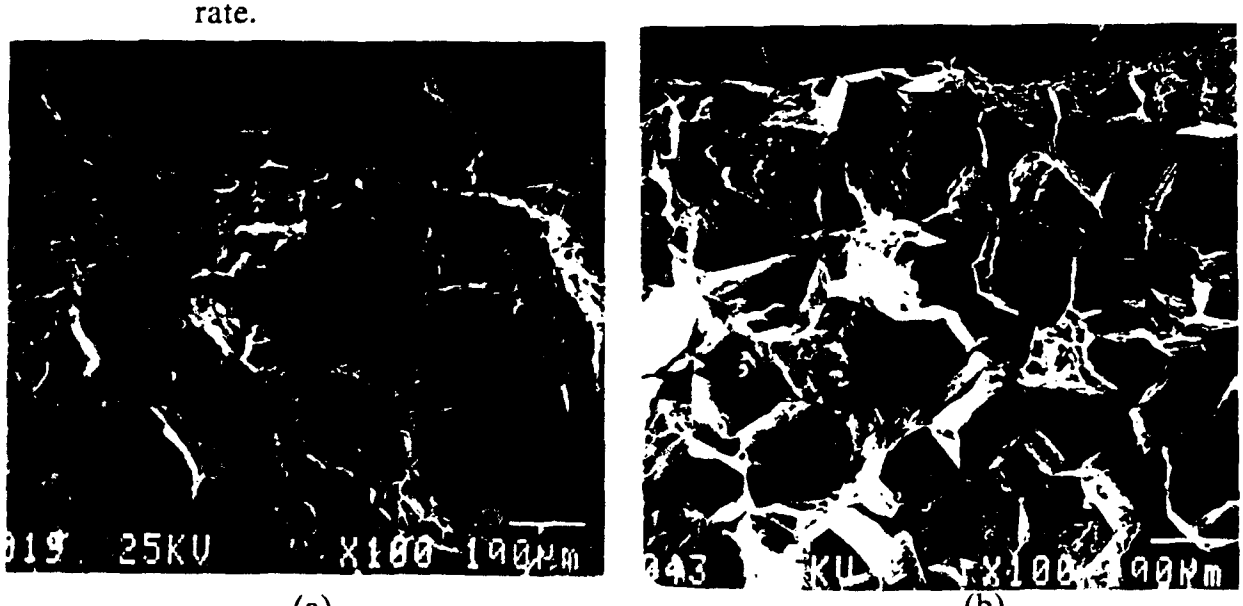

(a) (b)

Figure 6: SEM fractographs of the fatigue precrack (top) and rising load fracture toughness crack surfaces in Beta 21S: (a) air; (b) deaerated 3.5% NaCl.

Discussion

Fracture Toughness: Moist Air The moist air fracture toughnesses of Ti-15-3 (K_{IC} = 57 to 59 MPa$\sqrt{m}$) and Beta 21S (K_{IC} = 66 to 68 MPa$\sqrt{m}$) are comparable to values reported for ß-titanium alloys at similar yield strengths [25-27]. This agreement suggests that the K-Δa approach, coupled with DCPD detection of the onset of cracking, accurately characterizes plane strain fracture toughness in spite of insufficient specimen thickness compared to the requirement of ASTM Standard E399 (thickness > 2.5 $[K_{IC}/\sigma_{ys}]^2$).

The fracture toughness of Beta 21S is superior to that of Ti-15-3, particularly considering the higher yield strength of the former. The higher toughness of Beta 21S is curious because cracking of Beta 21S in moist air appears to involve grain boundary fracture. As confirmed in a later section, Beta 21S contains substantial α precipitates on ß grain boundaries, while this microstructure is not observed for Ti-15-3. Lee et al. and Froes et al. report that K_{IC} is degraded by grain boundary α [26,27]. A mechanism for this effect is localized plastic deformation in large low strength α plates, resulting in stress/strain concentrations and microvoid nucleation at α/ß interfaces near ß grain boundaries. Large grain size increased both the yield strength and fracture toughness of Ti-15-3 because of more homogeneous α precipitation resulting in decreased grain boundary deformation and fracture [28]. Inaba et al. report that tensile strength is independent of grain size, while elongation increases with decreasing ß grain size for constant α size and distribution [29]. These authors argue that fine ß grains suppress grain boundary fracture. The fracture toughness of Beta 21S may be improved by thermomechanical processing to eliminate α precipitates at ß grain boundaries.

Environmental Cracking Resistance The HEAC resistance of Ti-15-3 (K_{th} = 61 to 65 MPa$\sqrt{m}$ at σ_{ys} = 1040 MPa) is consistent with results reported by Rosenberg [4] and Bania [1]. K_{th} for this strength level of tempered martensitic steel in aqueous chloride may be as low as 38 MPa$\sqrt{m}$, but typically equals 65 MPa$\sqrt{m}$, depending on metallurgical variables (eg., metalloid impurity content) and mechanical variables such as loading rate or experiment duration [15]. Ti-15-3 may be embrittled by more aggressive hydrogen producing environments, including NaCl water with applied anodic or cathodic polarization and with sulfide additions [7,12,13,15]. Experiments are in progress to investigate this speculation.

It is hypothesized that ß-titanium alloys are embrittled by hydrogen environments when subjected to loading conditions that continuously destabilize the crack tip passive film to promote hydrogen entry [17]. Ripple loading, or low amplitude high frequency fatigue cycling, could be effective in this regard [30,31]. An experiment was conducted with Ti-15-3 in 3.5% NaCl at -600 mV_{sce}. The edge cracked tension specimen was loaded at several constant K levels with either no superimposed cyclic load, or with a ripple load characterized by a stress intensity range ($\Delta K = K_{max} - K_{min}$) of 0.8 MPa$\sqrt{m}$ applied at a frequency of 15 Hz. This ΔK is well below the measured threshold ΔK for fatigue crack propagation in vacuum (ΔK_{th} = 4 MPa$\sqrt{m}$ at K_{min}/K_{max} of 0.84 and operationally defined at a growth rate of 10^{-10} m/cycle) and is consistent with the notion that cyclic loading could disrupt a crack tip passive film due to high surface cyclic plastic strains (of order 0.1 to 0.5), but should not cause process zone volume fatigue damage because the cyclic plastic zone size is small (0.02 μm) [32]. DCPD measurements presented in Fig. 7 indicate that the fatigue precrack did not grow during constant load exposure in NaCl

for six-24 hour intervals of progressively increased constant K levels of 35, 45, and 55 MPa√m, and with alternating static and ripple loading. (Note the expanded y-axis. Average crack growth increments of less than 0.05 mm are readily resolvable with the electrical potential method.) The resistance of this strength level of Ti-15-3 to HEAC is further established for a wider range of crack tip strain rates.

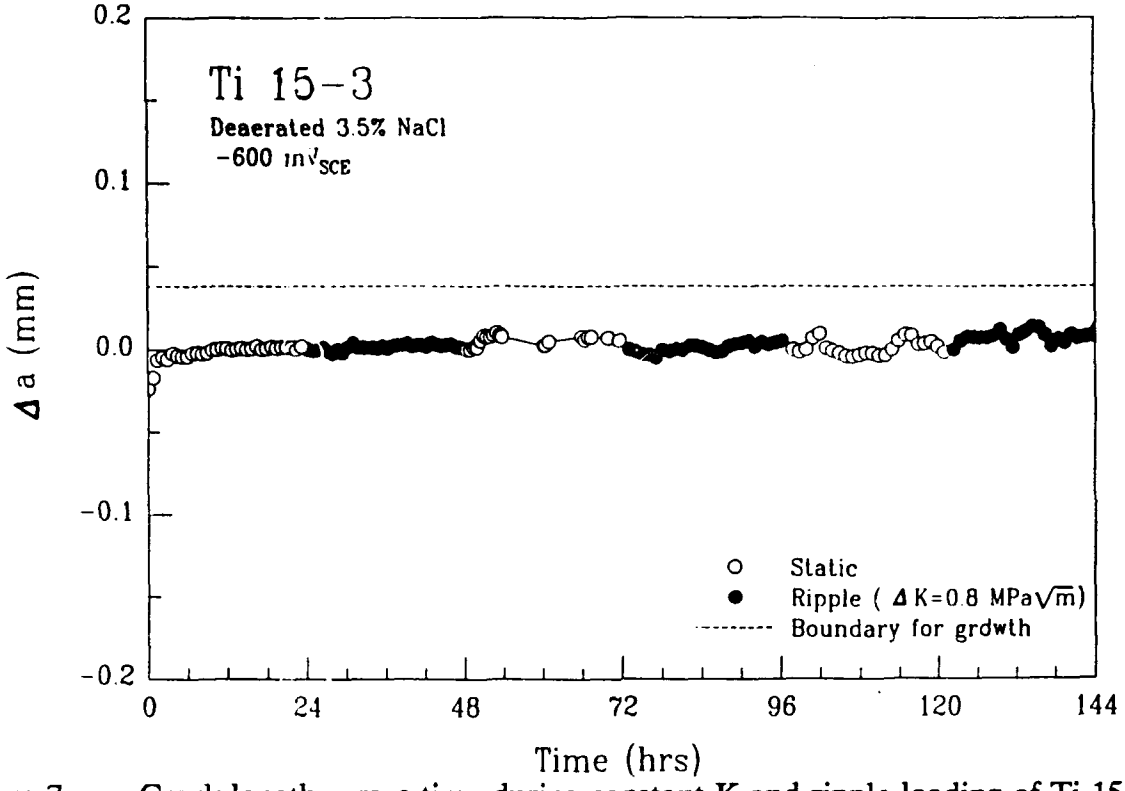

Figure 7: Crack length versus time during constant K and ripple loading of Ti-15-3 in 3.5% NaCl at -600 mV_{sce}.

The HEAC resistance of Ti-15-3 may be explained by yield strength; higher strength alloys are generally more susceptible to HEAC [15]. Gagg and Toloui report that Ti-15-3, aged at 510°C (σ_{ys} = 1200 MPa), is embrittled during slow strain rate loading of smooth tensile specimens in several chloride solutions [12]. The importance of σ_{ys} is further supported by the observed HEAC of Beta 21S (K_{th} = 38 MPa√m at σ_{ys} = 1200 MPa). K_{th} for this strength level of tempered martensitic steel in aqueous chloride is as low as 20 MPa√m and typically equals 36 MPa√m [15]. The effect of yield strength has not been systematically determined for ß-titanium alloys [11]. Ti-15-3 is easily hardened to 1300 MPa yield strength by aging at lower temperatures (500°C), however, the benign environment fracture toughness will likely decrease [1].

As an alternative to the hypothesized effect of σ_{ys}, the contrasting HEAC behavior of Ti-15-3 and Beta 21S may be traced to a microstructural mechanism. Optical and scanning electron microscopy of Beta 21S specimens, underaged for two hours at 538°C, reveals α precipitate nucleation and growth primarily on ß grain boundaries, as shown in Fig. 8a. Figure 8b shows that α does not preferentially nucleate on the ß grain boundaries of underaged Ti-15-3. For peak age, Ti-15-3 exhibits a homogeneous distribution of fine α platelets throughout each grain, while Beta 21S exhibits fine intragranular α plates and grain boundary α. Intragranular α precipitation is promoted by either post-solution treatment cold work, or by microstructures that are only partially recovered and recrystallized during solution treatment after hot rolling [33]. The

difference in solution treatment times, 8 hours for Beta 21S and 30 minutes for Ti-15-3, may enhance intragranular precipitation for the latter material. As-received Ti-15-3 was resolutionized (1038°C for 2 hours) for full recovery and recrystallization. Metallography of the underaged condition reveals preferential α nucleation at grain boundaries, Fig. 9, similar to Beta 21S.

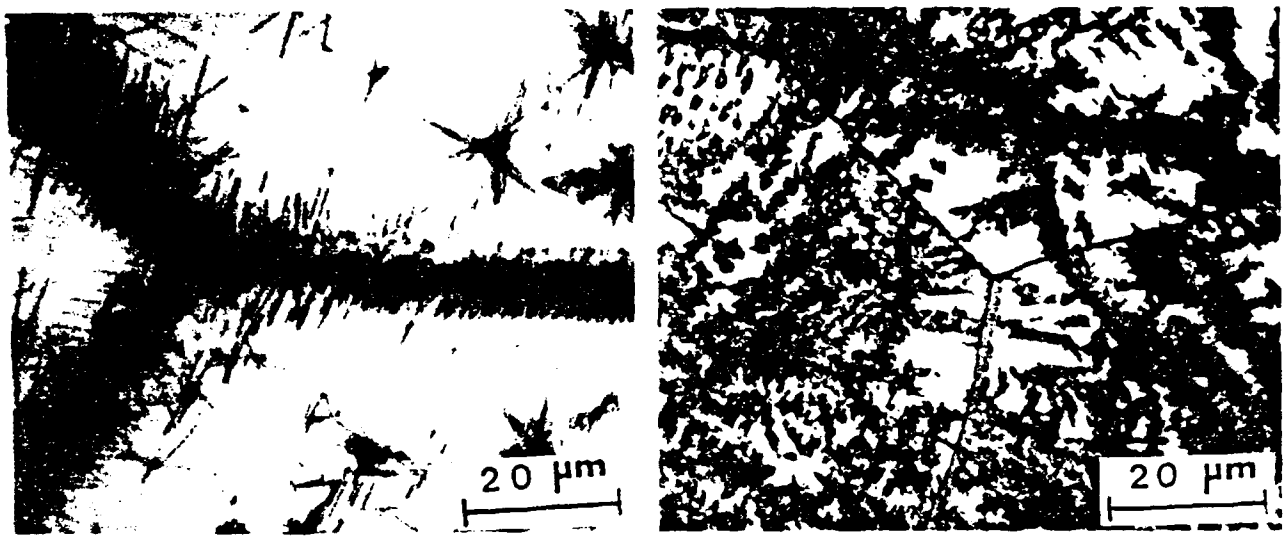

(a) (b)

Figure 8: Optical micrographs of underaged ß-titanium alloys: (a) Beta 21S showing grain boundary α nucleation; (b) Ti-15-3 showing predominantly intragranular α precipitation.

Figure 9: Optical micrograph of resolutionized and underaged Ti-15-3, showing grain boundary α nucleation, similar to underaged Beta 21S.

It is reasonable to speculate that the Beta 21S microstructure is sensitive to intergranular HEAC in aqueous chloride because of the extensive grain boundary α plates. This low energy fracture path may be preferred due to the formation of a brittle continuous hydride film, known to form in hcp α-titanium and at α/ß interfaces [5,7,34]. Additionally, localized plastic deformation in the α phase can result in high stress/strain concentrations at α/ß interfaces; microcracking could nucleate when such stresses

interact with embrittling hydrogen that is trapped at these interfaces. The idea that unrecrystallized titanium alloys exhibit improved stress corrosion cracking resistance was suggested as early as 1970 by Blackburn et al. [7]. Either cold rolling of Beta 21S prior to aging, or restricted recrystallization during solution treatment, should provide intragranular nucleation sites for α precipitates other than β grain boundaries. The more homogeneous microstructure could be resistant to HEAC. This speculation has not been experimentally confirmed, nor has sufficient research been conducted to unambiguously define the mechanism for HEAC.

The relative HEAC behaviors of Ti-15-3 and Beta 21S are not explained by simple expectations of occluded crack solution hydrogen production and uptake. Cr and V solute in the β phase of Ti-15-3 should anodically dissolve and hydrolyze to produce a more acid crack tip pH compared to Beta 21S which contains Mo and Nb. Additionally, it is reasonable to expect that Mo should promote crack tip passivity and hinder hydrogen uptake in Beta 21S. These hypotheses are not consistent with the measured HEAC resistance of the two alloys. Detailed crack chemistry, passivation and hydrogen permeation experiments are underway to examine these issues [17].

Loading rate affects the severity of HEAC for Beta 21S. As reported for several α/β and β-titanium alloys including Ti-15-3, embrittlement is maximized at an intermediate loading rate [7,12,35]. This trend is observed for Beta 21S; K_{th} is minimal at an actuator displacement rate of 0.025 mm/min. From the HEAC perspective, embrittlement is most severe at the loading rate that balances surface film destabilization (promoted by increased loading rate) with the time necessary for hydrogen diffusion into the crack tip process zone (promoted by decreased loading rate). The detailed kinetics of each process are not defined.

HEAC is likely governed by the crack tip strain rate, ($d\epsilon_{CT}/dt$), a quantity that is difficult to precisely define. As an approximation for monotonic loading of a stationary crack in an elastic-perfectly plastic material [32]:

$$d\epsilon_{CT}/dt = P\,(dP/dt)\,[2/(3B^2W^2E\sigma_{ys}X_o)]\,[a\,f(a/W)^2]$$

where P is load, dP/dt is loading rate, B is specimen thickness, W is specimen width, a is crack length, f(a/W) is a known geometric term [22], E is Young's modulus, σ_{ys} is yield strength and X_o is distance ahead of the crack tip. The problems in evaluating crack tip strain rate are the distance dependence, the uncertain value of X_o within the crack tip process zone, and the fact that strain rate increases linearly with load to crack initiation. We assume that the governing crack tip strain rate is the value at K equals K_{th}, and that X_o equals one blunted crack tip opening displacement (CTOD = $K^2/2\sigma_{ys}E$ [32,36]). Table 1 shows calculated crack tip strain rates for each experiment with Beta 21S and Ti-15-3. During the ripple load experiment with Ti-15-3, the average crack tip strain rate equals 0.2 sec^{-1} for X_o of 0.02 μm [32]. X_o is selected to equal the cyclic plastic zone diameter from the ripple load.

For Beta 21S, the crack tip strain rate is $< 10^{-5}$ sec^{-1} at displacement rates where K_{th} is lowest. From the literature for high strength Ti-15-3 in 0.2M NaCl at the open circuit potential (about -500 mV_{sce}), the smooth specimen strain rate for maximum

embrittlement was reported to equal between 2×10^{-6} and 8×10^{-6} sec^{-1} [12]. This value is on the order of the crack tip result for Beta 21S, however, each strain rate is sufficiently uncertain to preclude specific conclusions.

Table 1: Crack Tip Strain Rates for Rising Load Cracking of ß-titanium Alloys

Alloy/Environment	Actuator Displacement Rate (mm/min)	Crack Tip Strain Rate[3] (sec^{-1})
Ti-15-3/Air	0.0254	3×10^{-4}
Ti-15-3/NaCl	0.0254	2×10^{-4}
	0.00127	2×10^{-5}
	0.000254	1×10^{-6}
Beta 21S/Air	0.0254	2×10^{-4}
Beta 21S/NaCl	0.127	1×10^{-3}
	0.0254	4×10^{-4}
	0.00127	2×10^{-5}
	0.000254	4×10^{-6}

When loaded in aqueous chloride, each ß-titanium alloy displayed a strain rate sensitive crack bursting phenomenon. Because this effect was not observed during stable crack growth in moist air, discontinuous cracking may indicate that hydrogen diffusion from the crack tip surface to process zone damage sites is a requisite for discontinuous crack advance. For Beta 21S, the K-Δa data in Fig. 5a, and the corresponding crack length versus time data in Fig. 10, show that the resolved crack bursts are pronounced for the slowest loading rate and are eliminated for the fastest rate. Presumably, loading rate insensitive dislocation transport does not augment bulk hydrogen diffusion, which is insufficient to provide embrittling hydrogen above a limiting crack tip strain rate. Considering the case in Fig. 10, the times between the first (A, crack at K_{th}) and second (B) and second (B) and third (E) crack jumps are 4.3 and 6.2 hours, and the jump distances are 50 μm (A), 360 μm (B) and over 2000 μm (E) based on electrical potential measurements. The last large jump is probably unstable fracture at high K, and is not relevant to HEAC. The results in Fig. 10 show continuous crack growth at rates of 2×10^{-4} and 1×10^{-3} mm/min between the ab and bc events. If discontinuous cracking occurred within these regions, Δa was less than the resolution of the DCPD system, about 25 μm.

Crack burst times and distances can be compared to hydrogen diffusion ahead of the crack tip. Approximately 70 seconds are required for atomic hydrogen to diffuse a distance of two blunted crack tip opening displacements (9 μm) at K_{th}, and 15 minutes are required for transport to the boundary of the crack tip plastic zone (35 μm based on finite element analysis [36]). (These calculations assume a hydrogen diffusivity in ß-titanium of 5×10^{-8} cm^2/sec, with the diffusion distance approximated by $0.5[D_H t]^{1/2}$,

[3]Strain rates in the original paper were in error and are corrected here.

where t is time). The resolved jump distances are much larger than the high hydrostatic stress region approximated by twice CTOD. Finer scale discontinuous cracking within the plastic zone may not have been resolved by DCPD measurements. There is no compelling continuum mechanics explanation for HEAC growth over the entire plastic zone or beyond because of the reduction in tensile stress between the crack tip (of order $3\sigma_{ys}$ at 2 CTOD) and the plastic-elastic boundary (1.5 to $2\sigma_{ys}$ based on finite element analysis [36]). Large jumps suggest that the ß grain size plays a role in discontinuous HEAC, perhaps because high stress and local trapped hydrogen concentration must be exceeded over at least one grain. As an example, 2 hours are required for hydrogen to diffuse a distance of one grain diameter (100 μm) at a diffusivity of 5 x 10^{-8} cm^2/sec. (While grain boundary hydrogen diffusion is normally rapid, extensive α precipitates in Beta 21S may slow hydrogen diffusion and complicate the mass transport analysis.) This time is not unreasonable compared to the experimental measurements. Exact hydrogen diffusivities and the time-distance continuity of HEAC in ß-titanium alloys must be determined, and a detailed micromechanical model of process zone hydrogen uptake and embrittlement must be developed.

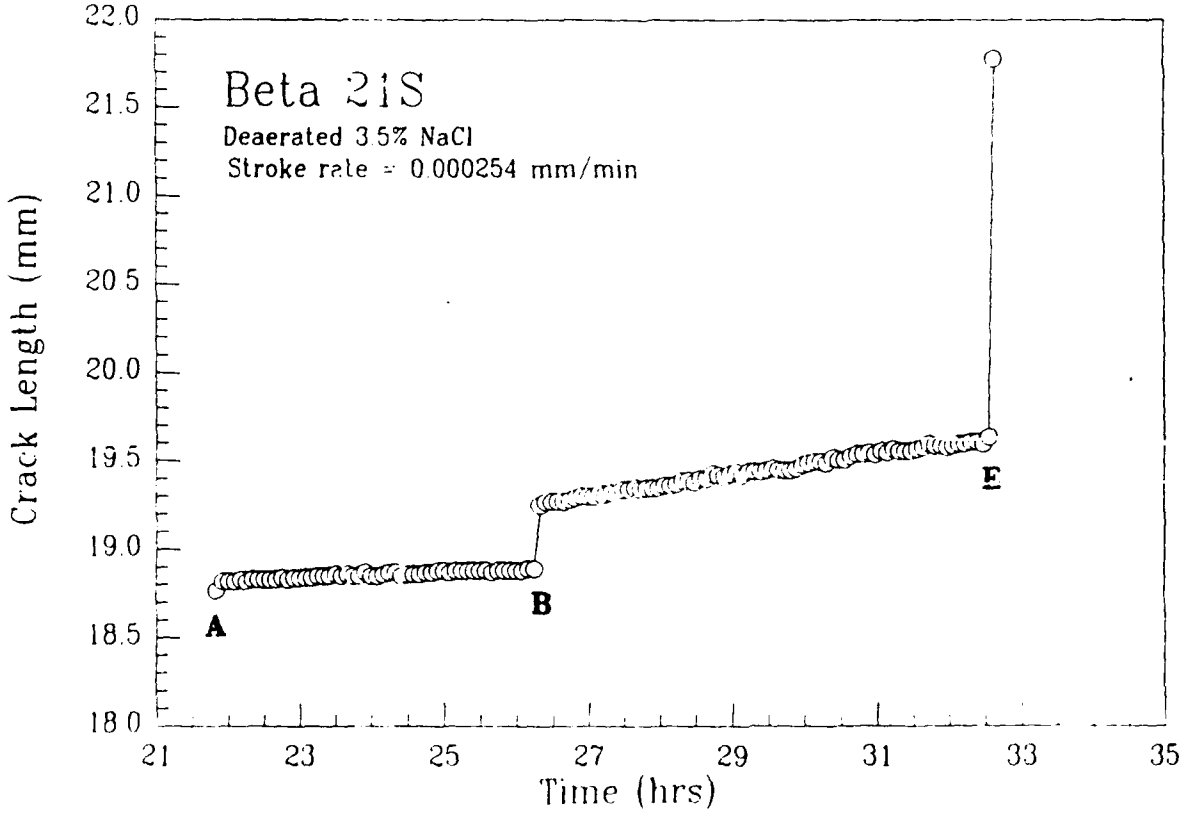

Figure 10: Crack length from DCPD measurements versus time during slowly rising loading (0.00025 mm/min) of Beta 21S in 3.5% NaCl at -600 mV_{sce}.

Conclusions

1. The threshold stress intensity for stable crack propagation in Beta 21S is significantly reduced by simultaneous slow rising loading and exposure to aqueous NaCl at -600 mV_{sce}. Crack propagation, presumably by a hydrogen embrittlement mechanism, involves intergranular separation for chloride compared to grain boundary microvoid processes for moist air.

2. The crack initiation fracture toughness and microscopic fracture processes of Ti-15-3 are unaffected by hydrogen environment exposure for several slow constant actuator displacement rates, constant load, and a high frequency ripple load condition designed to destabilize the crack surface film without causing process zone volume fatigue damage.

3. The moist air fracture toughnesses and chloride environmental cracking thresholds of Ti-15-3 and Beta 21S are similar to the behavior of tempered martensitic steels at equal yield strengths.

4. The hydrogen environment assisted cracking (HEAC) susceptibility of Beta 21S and the resistance of Ti-15-3 are explained based on the high yield strength and copious α precipitation on β grain boundaries of the former alloy.

5. Dynamic loading rate strongly affects HEAC in Beta 21S; the threshold for crack growth in NaCl is possibly minimized at a crack tip strain rate of order 10^{-5} sec^{-1}.

6. Crack propagation is discontinuous (50 to 360 μm jumps) for Beta 21S and Ti-15-3, only in NaCl, suggesting time dependent development of a critical crack tip process zone hydrogen concentration-tensile stress condition.

Acknowledgements

This research was supported by the Office of Naval Research (Grant N00014-91-J-4164) with Dr. A. John Sedriks as Scientific Monitor, and by the Virginia CIT Center for Electrochemical Science and Engineering at the University of Virginia. Material was donated by the Titanium Metals Corporation. This support is gratefully acknowledged, as are discussions with Dr. J.R. Scully and Messrs G. Young and D. Kolman.

References

1. P.J. Bania, G.A. Lenning, and J.A. Hall, "Development and Properties of Ti-15V-3Cr-3Sn-3Al (Ti-15-3)", in Beta Titanium Alloys in the 80's, R.R. Boyer and H.W. Rosenberg, eds., TMS-AIME, Warrendale, PA, pp. 209-229, 1983.
2. J.S. Grauman, "Beta-21S: A New High Strength, Corrosion Resistant Titanium Alloy", presented at the 1990 TDA International Conference, Orlando, Fl, 1990.
3. P.J. Bania and W.M. Parris, "Beta-21S: A High Temperature Metastable Beta Titanium Alloy", presented at the 1990 TDA International Conference, Orlando, Fl, 1990.
4. H.W. Rosenberg, "Ti-15-3 Property Data", in Beta Titanium Alloys in the 80's, R.R. Boyer and H.W. Rosenberg, eds., TMS-AIME, Warrendale, PA, pp. 409-432, 1983.
5. T.W. Duerig and J.C. Williams, "Overview: Microstructure and Properties of Beta Titanium Alloys", in Beta Titanium Alloys in the 80's, R.R. Boyer and H.W. Rosenberg, eds., TMS-AIME, Warrendale, PA, pp. 19-67, 1983.
6. R.J.H. Wanhill, "Aqueous Stress Corrosion in Titanium Alloys", British Corrosion Journal, Vol. 10, No. 2, pp. 69-78, 1975.

7. M.J. Blackburn, J.A. Feeney, and T.R. Beck, "Stress Corrosion Cracking of Titanium Alloys", in Advances in Corrosion Science and Technology, M.G. Fontana and R.W. Staehle, eds., Vol. 3, Plenum Publishing, NY, NY, pp. 67-292, 1972.
8. R.W. Schutz and D.E. Thomas, "Corrosion of Titanium and Titanium Alloys", in Corrosion; Metals Handbook, Vol. 13, Ed. 9, ASM International, Metals Park, OH, pp. 669-706, 1987.
9. D.N. Fager and W.F. Spurr, "Some Characteristics of Aqueous Stress Corrosion in Titanium Alloys", Trans. ASM, Vol. 61, pp. 283-292, 1968.
10. J.A. Feeney and M.J. Blackburn, "Effect of Microstructure on the Strength, Toughness, and Stress Corrosion Susceptibility of a Metastable Titanium Alloy", Met. Trans., Vol. 1, pp. 3309-3323, 1970.
11. Corrosion; Metals Handbook, Vol. 13, Ed. 9, ASM International, Metals Park, OH, pp. 483-485, 1987.
12. C. Gagg and B. Toloui, "The Biocompatibility, Mechanical and Electrochemical Properties of Ti-15-3", in Sixth World Conf. on Titanium, pp. 545-550, 1988.
13. D.E. Thomas and S.R. Seagle, "Stress Corrosion Cracking Behavior of Ti-38-6-44 in Sour Gas Environments", in Titanium Science and Technology, Vol. 4, G. Lutjering, U. Zwicker and W. Bunk, eds., pp. 2533-2540, 1984.
14. N.E. Paton, R.A. Spurling and C.G. Rhodes, "Influence of Hydrogen on Beta Phase Titanium Alloys", in Hydrogen Effects in Metals, I.M. Bernstein and A.W. Thompson, eds., TMS-AIME, Warrendale, PA, pp. 269-279, 1981.
15. R.P Gangloff, "A Review and Analysis of the Threshold for Hydrogen Environment Embrittlement of Steel", in Corrosion Prevention and Control, M. Levy and S. Isserow, eds., US Army Laboratory Command, Watertown, MA, pp. 64-111, 1986.
16. W.W. Gerberich, N.R. Moody and C.L. Jensen, "Hydrogen in α/β and All β-Titanium Systems", in *Hydrogen Effects in Metals*, I.M. Bernstein and A.W. Thompson, eds., TMS-AIME, Warrendale, PA, pp. 731-745, 1981.
17. R.P. Gangloff and J.R. Scully, "Mechanisms for the Environmental Cracking Resistance of High Strength Titanium Alloys", Proposal No. MS-DOD/ONR-4956-91, University of Virginia, Charlottesville, VA, 1991.
18. S. Ankem and S.R. Seagle, "Heat Treatment of Metastable Beta Titanium Alloys", in Beta Titanium Alloys in the 80's, R. R. Boyer and H. W. Rosenberg, eds., TMS-AIME, Warrendale, PA, pp. 107-126, 1983.
19. D.R. Anderson and J.P. Gudas, "Stress Corrosion Evaluation of Titanium Alloys Using Ductile Fracture Mechanics Technology", in Environment Sensitive Fracture: Evaluation and Comparison of Test Methods, ASTM STP 821, S.W. Dean, E.N. Pugh and G.M. Ugiansky, eds., ASTM, Philadelphia, PA, pp. 98-113, 1984.
20. E.M. Hackett, P.J. Moran and J.P. Gudas, "Evaluation of Environmentally Assisted Cracking of a High Strength Steel Using Elastic-Plastic Fracture Mechanics Techniques", in Fracture Mechanics: Seventeenth Volume, ASTM STP 905, J.H. Underwood, et al., eds., ASTM, Philadelphia, PA, pp. 512-541, 1986.
21. R.A. Mayville, T.J. Warren and P.D. Hilton, "Influence of Displacement Rate on Environmentally Assisted Cracking of Precracked Ductile Steel Specimens", Trans. ASME, Vol. 109, pp. 188-193, 1987.
22. H. Tada, P.C. Paris and G.R. Irwin, The Handbook, Del Research Corp., St. Louis, MO, p. 2.11, 1985.

23. J.K. Donald and J. Ruschau, "Direct Current Potential Difference Fatigue Crack Measurement Techniques", Fatigue Crack Measurement: Techniques and Applications, K.J. Marsh, R.A. Smith and R.O. Ritchie, eds., EMAS, Ltd, West Midlands, UK, pp. 11-37, 1991.
24. P. Doig and K.R. Abbott, "Single Specimen Fracture Toughness Testing of Low Strength Steel Plate Using the Direct Current Electrical Potential Method", J. Test. Eval., Vol. 12, pp. 297-304, 1984.
25. R.R. Boyer, "Design Properties of a High Strength Titanium Alloy, Ti-10V-2Fe-3Al", J. Metals, March, pp. 61-65, 1980.
26. C.S. Lee, S.J. Kim, C.G. Park and Y.W. Chang, "Effect of Microstructural Variation on the Mechanical Properties of Ti-10V-2Fe-3Al", private communication, 1992.
27. F.H. Froes, J.C. Chesnutt, C.G. Rhodes and J.C. Williams, "Relationship of Fracture Toughness and Ductility to Microstructure and Fractographic Features in Advanced Deep Hardenable Titanium Alloys", in Toughness and Fracture Behavior of Titanium, ASTM STP 651, ASTM, Philadelphia, PA, pp. 115-153, 1978.
28. E. Breslauer and A. Rosen, "Relationship Between Microstructure and Mechanical Properties in Metastable ß-titanium 15-3 Alloy", Matls. Sci. and Tech., Vol. 7, pp. 441-446, 1991.
29. T. Inaba, K Ameyama and M. Tokizane, "Effects of ß Grain Size and Morphology of α Precipitate on the Mechanical Properties of Ti-15V-3Cr-3Sn-3Al", J. Japan Inst. Metals, Vol. 54, pp. 853-860, 1990, in Japanese.
30. G.R. Yoder, P.S. Pao and R.A. Bayles, "Ripple-Load Cracking in a Titanium Alloy", Scripta Metallurgica et Materialia, Vol. 24, pp. 2285-2289, 1990.
31. P.S. Pao and R.A. Bayles, "Effect of Ripple Load on Stress Corrosion Cracking in Structural Steels", NRL Publication 190-6320, Naval Research Laboratory, Washington, DC, 1991.
32. R.P. Gangloff, "Corrosion Fatigue Crack Propagation in Metals", in Environment Induced Cracking of Metals, R.P. Gangloff and M.B. Ives, eds., NACE, Houston, TX, pp. 55-109, 1990.
33. J.C. Williams, "Critical Review: Kinetics and Phase Transformations", in Titanium Science and Technology, R.I. Jaffee and H.M. Burte, eds., TMS-AIME, New York, pp. 1433-1494, 1973.
34. J.E. Costa, D. Banerjee and J.C. Williams, "Hydrogen Effects in ß-Titanium Alloys", in Beta Titanium Alloys in the 80's, R.R. Boyer and H.W. Rosenberg, eds., TMS-AIME, Warrendale, PA, pp. 69-84, 1983.
35. J.A. Muskovitz and R.M. Pelloux, "Dependence of K_{ISCC} on Loading Rate and Crack Orientation in Ti-6Al-6V-2Sn", Corrosion, Vol. 35, pp. 509-514, 1979.
36. J.F. Knott, Fundamentals of Fracture Mechanics, John Wiley and Sons, New York, NY, pp. 86-90, 1979.

Intended for submission to: Metallurgical Transactions

THE INFLUENCE OF HYDROGEN ON THE MECHANICAL PROPERTIES OF TIMETAL 21S

George A. Young Jr. and John R. Scully
Department of Materials Science and Engineering
The University of Virginia
Charlottesville, VA 22903

Abstract

The effects of internal hydrogen on the room temperature mechanical properties of the peak aged beta titanium alloy, TIMETAL 21S, are quantified as functions of stress and strain state in Bridgman notched tensile bars. Electrochemical precharging of hydrogen into previously aged material is employed to preserve a fully aged microstructure. Hydrogen effects are decoupled from aqueous embrittlement phenomena via mechanical testing of pre-charged material in air. Maximum longitudinal stress and plastic strain at maximum load decrease with increasing hydrogen concentrations ranging from 10-3000 ppm. The decrease is more pronounced at the higher constraint levels. Fracture path is shown to be a function of hydrogen concentration and level of constraint. Both transgranular and intergranular fracture are observed. Intergranular separation is attributed to high levels of hydrogen and constraint and possibly to preferential α precipitation on grain boundaries. X-ray diffraction analysis of the failed notched regions detected no evidence of hydride formation in the subsurface α phase.

Introduction

Critical aerospace, petrochemical, and marine applications demand high strength, formable materials which are resistant to corrosion, stress corrosion, and hydrogen embrittlement. Modern β titanium alloys are candidates for many such applications due to their excellent strength, toughness, formability, and resistance to general corrosion [1-5]. Furthermore, titanium's compact surface oxide film limits hydrogen entry and the underlying β matrix has a high solubility for hydrogen [6-7]. However, both model binary beta titanium alloys as well as early developmental β alloys (Ti-13V-11Cr-3Al) can be susceptible to hydrogen embrittlement. Shih and Birnbaum have shown that the solution treated beta alloy Ti-30 Mo is extrinsically embrittled through the formation of the fcc δ hydride containing 66 at% hydrogen [8]. Solution treated beta alloys are also intrinsically embrittled by hydrogen at bulk concentrations well below that required to produce hydriding of the β matrix [9-10]. Gerberich, et al., have shown a continuous decrease in the fracture stress of solution annealed Ti-30 Mo containing 20-1800 ppm by weight of hydrogen without the formation of a hydride [11]. Nakasa and co-workers studied Ti-13V-11Cr-3Al and found a decrease in bending strength for both the solution annealed and peak-aged conditions, again without detection of hydriding in either the α or β phases at hydrogen concentrations up to 15,000 wt. ppm. A {100} cleavage plane was identified on flat fracture surfaces in both the solution annealed and aged conditions. The fct hydride was detected only under extreme autoclave conditions at hydrogen concentrations of the order of 40,000 ppm [12]. Hydrogen was also implicated in the aqueous cracking of aged β-titanium alloy Beta-C (Ti-3Al-8V-6Cr-4Mo-4Zr) [13]. In this study, embrittlement was only observed when pre-cracked specimens were cathodically polarized in H_2S containing acidified chloride solutions. Other studies of α-β and metastable β-titanium alloys in aqueous solutions also attribute embrittlement to

a hydrogen environment assisted cracking mechanism [14-16]. Coincidentally, a {100} cleavage plane [17] as well as intergranular separation [16,17] are observed. Factors supporting a time dependent hydrogen embrittlement phenomena for TIMETAL 21S in aqueous solutions include (a) electrochemical conditions at the crack tip which favor hydrogen production, (b) a loading rate dependency, (c) and discontinuous crack bursts [16].

Current understanding of the controlling hydrogen embrittlement mechanisms in peak aged, β-titanium alloys is insufficient to enable critical, damage tolerant applications [18]. The present research seeks to define the effects of a range of internal hydrogen concentrations on the room temperature mechanical properties of the peak aged, beta titanium alloy TIMETAL 21S and to correlate hydrogen assisted fracture paths to those observed in aqueous, environmentally assisted cracking [16]. Here, electrochemical pre-charging, near ambient temperature, of previously aged material is conducted to avoid the complications of hydrogen induced β phase stabilization common to high temperature gaseous charging studies [19-21]. Mechanical testing of pre-charged specimens is performed in air, to decouple hydrogen effects from other aqueous embrittlement mechanisms. Embrittlement is quantified as a function of maximum longitudinal stress, plastic strain at maximum load, and hydrogen concentration. Hydriding of the α and β phases is investigated through x-ray diffraction. Metallographic and fractographic features are correlated with mechanical property data and likely fracture scenarios discussed. Hydrogen assisted fracture paths are compared to aqueous, EAC fracture modes.

Experimental

Solution annealed, cross-rolled β 21S plate, nominally 10 mm thick was received from TIMET. The solution treated condition was 871 °C for 8 hours followed by an air cool. Vendor reported chemistries are given in Table 1. Heat treatment of as-received plate consisted of an 8 hour age, in air, at 538° C, followed by an air cool, as recommended by the vendor. One hour and eight hour aged microstructures are shown in Figure 1. Note that α precipitates nucleate preferentially on β grain boundaries after the 1 hour age but the α-β distribution has homogenized after 8 hours. Hardness for the eight hour, "peak aged" condition was approximately R_c 42 +/-1.2. Yield strengths corresponding to this aging condition are approximately 1205-1380 MPa [4,22].

X-ray diffraction patterns of solution annealed and peak aged β 21S plate were taken with a Scintag automated diffractometer. Copper K-α radiation was continuously scanned over 30-80 ° 2Θ at a rate of 1° per minute. Figure 2 shows the pure β structure of solution annealed material and the α + β peaks in peak aged material. For uncharged material with a residual hydrogen level of approximately 80 wt. ppm H, a BCC lattice parameter of 0.325 nm was obtained in good agreement with Hayman and Gerberich who obtained 0.3247 nm for "aged" Ti-30 Mo [23]. Phases such as ω or β' are not detected but further TEM studies are required to confirm this. Such phases have been observed in Beta C and Beta III alloys [24].

Aged plate was machined into circumferentially notched tensile bars. Electrochemical pre-charging of hydrogen was conducted at 90° C, in a solution of 10ml sulfuric acid, 1000ml H_2O and 0.8g sodium pyrophosphate. Machined specimens were cathodically polarized to 10 mA/cm^2 to promote hydrogen uptake and to provide cathodic protection (Figure 3) [25]. The method used to vary hydrogen concentration involved variation of charging time as opposed to charging current density. The rational for this

approach is two-fold. Firstly, the use of higher cathodic c.d.'s to achieve higher hydrogen concentrations may exacerbate selective surface spalling of α precipitates which apparently readily hydride [26]. Secondly, different overall hydrogen levels may be achieved using the time based approach because of diffusion controlled internal redistribution of dissolved hydrogen across the sample diameter [12,27]. In future work, thermal stimulation will be employed to insure homogeneous hydrogen distribution. This point will be discussed further below. It is important to note that egress of hydrogen while the specimen is exposed to air is significantly impeded for titanium due to the formation of an oxide film permeation barrier upon removal of specimens from the charging bath. Results of the hydrogen charging operations are summarized in Table 2, as analyzed by thermal emission methods (LECO).

Tensile tests were conducted with an Instron 1362 servo-hydraulic mechanical testing system in laboratory air at room temperature. Applied load, diametral strain, and time were continuously monitored with a PC based data acquisition system. Tensile bars were tested to failure immediately following hydrogen charging, at a constant stroke rate of 1.5×10^{-2} mm/min. The fracture surface was examined with the aid of a JEOL JXA-840 scanning electron microscope (SEM).

The effects of constraint on the failure stress and strain were investigated by employing Bridgman-type, circumferentially notched tensile bars to develop differing levels of net section triaxial constraint [28]. Constraint levels from 0.52 (0.33 = uniaxial tension) to 1.03 (2.5 = sharp notch) were investigated. Degree of embrittlement was quantified by determining the maximum longitudinal stress developed at the centerline of the notched region and the effective plastic strain across the notch diameter at maximum load [28-30]. Following the procedure of Hancock et. al. [29], maximum load was used as the comparison point since uncharged bars failed after achieving a maximum load as well as experiencing a load decrease, while hydrogen charged bars invariably failed at maximum load. The equations describing the maximum longitudinal stress, effective plastic strain, and degree of triaxiality are given in Figure 4.

Results

Mechanical Testing

For each constraint level investigated, hydrogen decreases the longitudinal stress developed at the centerline of the notch at maximum load and the effective plastic strain across the notch diameter. Both stress and strain decrease with increasing hydrogen concentration as shown in Figure 5. The hydrogen concentrations reported here were obtained from a section of each tensile bar near the notch and as such represent an average concentration for the volume of metal tested. Note that the effect of hydrogen concentration on applied stress is most pronounced for the notch with the greatest degree of triaxiality. The present test method does not readily distinguish crack nucleation from growth. A rising load fracture mechanics method will be employed in future work to define threshold stress intensities.

Fractography

Fracture mode changes with both hydrogen concentration and level of constraint. Four distinct fracture modes were observed; microvoid coalescence, two types of transgranular fracture, and intergranular fracture. Typical fractographs illustrating each

distinct fracture mode are shown in Figure 6.

At low hydrogen levels, microvoid rupture is the predominant fracture mode as occurs at room temperature in air. With increasing hydrogen content and constraint, a second transgranular, fracture mode containing microscopically ductile tearing features of the size of the alpha precipitates is activated (Transgranular 1). At hydrogen concentrations on the order of 3000 ppm and near uniaxial constraint levels, a second transgranular fracture mode was observed (Transgranular 2). Intergranular cracking was triggered only at hydrogen contents on the order of 2000 ppm and the highest degree of triaxiality investigated. Table 3 summarizes the relationship between fracture mode, hydrogen concentration, and constraint for both the notch edge and the axial centerline.

Inspection of Table 3 a) and b) reveal seemingly contradictory information. The intergranular fracture mode occurs near the edge of the specimen where the triaxial stress is lowest according to Bridgman's analysis [28-30]. In contrast, a fracture mode apparently requiring intermediate fracture energy (transgranular) is observed near the specimen centerline. However, these results are consistent with a hydrogen concentration profile which decreases from edge to center. Such a concentration profile was verified through determinations of the β lattice parameter at various depths from the precharged surface. These results imply a hydrogen diffusion coefficient below 1.3×10^{-6} cm^2/sec at 90 °C for aged TIMETAL 21S since a diffusion coefficient above this value would ensure completely uniform charging across the notch diameter in 24 hours, assuming diffusion controlled ingress. Holman et. al., obtained the following relationship for hydrogen diffusion in solutionized Ti-13V-11Cr-3Al: $D = 1.58 \times 10^{-3} \exp(-5140 \pm 300$ cal/mole / RT) [31]. This relationship yields a diffusion coefficient of 1.9×10^{-6} to 8.4×10^{-7} cm^2/sec at 90 °C. Holman's result is in good agreement with Adler's work on the solution annealed β-Ti alloy Ti-8Mo-8V-2Fe-3Al which reported $D = 8 \pm 2 \times 10^{-7}$ cm^2/sec at 25 °C [32]. It is clear from the present work that TIMETAL 21S has an apparent diffusion coefficient including a trapping effect of α precipitates, dislocation density, and other sites, which is significantly lower than solution annealed β-Ti alloys.

Despite, the non-uniform hydrogen concentration profile, the results shown in Table 2 point to the possibility of a critical stress - hydrogen concentration failure criterion. Although, the stress at the notch surface of the high constraint tensile bar is lower than the stress at the centerline by a factor of 0.59, the hydrogen concentration is appreciably greater. It is interesting to note that rising load fracture mechanics testing on β 21S in 3.5% NaCl produced discontinuous crack jumps of distances equal to two β grains ($\approx$200 μm) over time periods of several hours suggestive of diffusion controlled hydrogen transport in the fracture process zones [16]. The radial depth of the intergranular zone shown here was approximately 900 μm after charging for 64 hours. Both results independently imply a diffusion coefficient below 10^{-8} cm^2/second. Together, these results suggest that intergranular cracking is no longer favorable when a high hydrogen concentration does not exists in the fracture process zone over a distance equal to a multiple number of grains.

Detection of Hydride Formation

Analysis of XRD data from peak aged TIMETAL indicates a β phase lattice parameter of 0.325 nm for uncharged material ($\approx$75 $\pm$ 25 ppm), 0.328 for 24 hour charging ($\approx$1400 $\pm$ 400 ppm) and 0.331 nm for 64 hour charging ($\approx$2600 $\pm$ 800 ppm). Paton et al. correlated lattice parameter to hydrogen concentration in solution annealed Ti-18 Mo [33].

They obtained 0.328 and 0.331 nm at 1000 and 2100 ppm, respectively, in good agreement with the data presented here. No evidence of hydriding of the β phase was found.

Regarding the possibility of hydriding of the α precipitate, x-ray diffraction analysis was conducted on (a) specimen surfaces, (b) several micrometers beneath the specimen surface, and (c) at a position as near as possible to the centerline of notched region of the high constraint, high hydrogen condition. The latter two conditions were achieved by surface grinding and sectioning, respectively. Neither α nor β phase hydride formation were detected at either (a), (b) or (c). Instead, the peaks normally coinciding with the α precipitates are observed (Figure 7) except for immediately at the charged surface where neither the α phase nor its corresponding hydride are observed. Electron microscopic examination revealed that selective elimination of the α phase was due to spalling of the near surface α precipitates (Figure 8). Such spalling would be expected based on the volume change which occurs on hydriding [8]. To confirm the notion that surface α could be hydrided under the electrochemical conditions used here, commercially pure Ti was charged under identical conditions used for β 21S. Hydride formation was indeed confirmed by XRD. A spectra of a hydride powder is shown in Figure 8 along with the hydrided Grade 2 titanium. To summarize, our current findings suggest that hydriding of α precipitates occurs at the free surface but that the hydriding of a large volume fraction of the subsurface α is not prevalent. Instead, internal hydrogen partitions to the β phase.

Discussion

Interpretation of Observed Fracture Paths

Ductile fracture of uncharged specimens appear to follow void initiation, growth, and coalescence mechanisms. Large, equiaxed voids are often seen at globular (silicide-phosphide-type) inclusions which are connected by areas of finer voids oriented approximately 45° to the tensile axis. As hydrogen and constraint are increased to the "medium" levels investigated here, a second fracture mode is triggered as shown in Figure 5. This fracture mode, although containing regions which appear microscopically ductile, occurs with significantly less plasticity than uncharged specimens. The tearing features suggest that ductile separation of the α/β interfaces has occurred along with some trans-plate fracture. Hydrogen may segregate to these interfaces as a consequence of coherency strains or it may simply embrittle the surrounding β matrix. At similar constraint levels but higher hydrogen concentrations, the microscopic ductile tearing features disappear and a transgranular fracture mode containing small flat regions joined by ledges results. During this fracture process, the increased hydrogen content may embrittle the $\beta+\alpha$ structure to a degree which precludes ductile tearing of α-β interfaces. Instead, transgranular fracture of the α and β phases results with very limited plasticity. Both transgranular modes might be expected with sufficient dissolved hydrogen based on the literature which reports a transgranular fracture appearance for both solutionized and aged Ti-15-3-3 as well as Ti-13-11-3 at room temperature [12,34]. Moreover, for both solutionized and aged Ti-15-3-3 and "aged and partially resolutionized by dissolved hydrogen" β 21S, the ductile to brittle transition temperature inherent to bcc metals is observed to increase above room temperature with dissolved hydrogen [34,35]. Such "lower shelf" behavior has apparently been achieved in the present study at 25 °C.

Intergranular cracking, seen in both hydrogen and aqueous chloride testing of aged TIMETAL 21S [16] appears to occur only at a high degree of triaxiality and hydrogen

concentration. Preferential α precipitation at β grain boundaries (as seen in Figure 1) may provide a continuous path for localized hydriding and subsequent fracture. Although bulk hydriding of the α phase was not detected, it is possible that local hydriding of the α phase occurred at α/β interfaces [36]. Alpha titanium has a relatively small hydrogen solubility (approximately 80 ppm at 90 °C) [37] and stress assisted hydriding in α and α-β alloys is well established [38,39]. Hydrogen accumulation at α/β interfaces, which serve either as trap sites or site for local strain induced hydriding, could result in subsequent fracture along α-β interfaces. This multiple stage process is consistent with the intergranular crack bursting phenomena associated with a time for hydrogen accumulation [16]. Moreover, if the continuous grain boundary α is removed (as in TIMETAL 15-3 which does not exhibit preferential α precipitation along β grain boundaries) the alloy is immune to EAC in aqueous chloride testing [16]. The absence of intergranular cracking of high hydrogen, high constraint notched tensile specimens of aged TIMETAL 15-3 will be confirmed in future work. While intergranular fracture processes may involve local hydriding of the preferentially nucleated, grain boundary α phase or trapping at α/β interfaces, it is important to note that overall hydrogen embrittlement of β titanium alloys is not contingent on bulk α hydriding. Further evidence is the hydrogen embrittlement of solutionized β-Ti alloys [9-12].

Comparison of Hydrogen Embrittlement and Aqueous EAC Fractography

The high hydrogen, high constraint specimen produced an intergranular fracture mode which is notably similar to embrittled fracture surfaces produced in aqueous chloride testing of TIMETAL 21S [16]. Fractography from each type of testing is shown in Figure 10. for comparison. Similarities in fracture mode suggest that the same embrittlement mechanism may be operative for both types of tests. While fracture comparison is far from conclusive evidence of this, future work including testing compact tension specimens precharged with hydrogen, aqueous chloride testing as a function of crack tip strain rate, and determination of crack tip pH and chemistry, will help support or discount a hydrogen-EAC mechanism of embrittlement in peak aged β titanium alloys.

Conclusions

Peak aged TIMETAL 21S is embrittled by hydrogen concentrations well below those required to hydride the β phase. Fracture path is a function of both level of constraint and hydrogen concentration. Approximate ranking of fracture modes from toughest to most brittle is: microvoid rupture, transgranular tearing of α-β interfaces, transgranular fracture through the α-β microstructure, and intergranular fracture. Intergranular fracture was only produced at the highest constraint and hydrogen concentrations. Preferential α precipitation on β grain boundaries is suggested to have a detrimental role on HEAC since transgranular cleavage cracking is more typically observed for solutionized β. Alpha precipitates within the β matrix may hydride locally at α/β interfaces although no evidence of this was detected. Alternatively the α/β interface may serve as a trap site whose strength increases with increasing hydrogen concentration due to increased coherency strain. The resulting intergranular fracture morphology in the case of high hydrogen-high constraint, tensile specimens is similar to that observed in 3.5% NaCl at -600 mV, suggesting a hydrogen assisted mechanism for the latter.

Acknowledgements

This research was supported by the Office of Naval Research (Grant N00014-91-J-4164) with Dr. A. John Sedricks as Scientific Monitor and by the Virginia Center for Electrochemical Science and Engineering at the University of Virginia. Material was donated by the Titanium Metals Corporation. The authors wish to acknowledge the helpful discussions with L.M. Young, R.P. Gangloff, D.G. Kolman, and B. Somerday.

References

[1] H. G. Nelson, "Hydrogen Environment Effects on Advanced Alloys and Composites in Aerospace Structures", in First Thermal Structures Conference, E. Thornton, ed., Nov 13-15, The University of Virginia, Charlottesville, VA 22903, pp. 301-311 (1990).

[2] P.J. Bania, G.A. Lenning and J. A. Hall, "Development and Properties of Ti-15V-3Cr-3Sn-3Al (Ti-15-3)", in Beta Titanium Alloys in the 80's, R.R. Boyer and H.W. Rosenberg eds., TMS-AIME, Warrendale, PA, pp. 209-229, (1983).

[3] A.G. Hicks and H. W. Rosenberg, "Ti-15-3 Foil Properties and Applications", in Beta Titanium Alloys in the 80's, R.R. Boyer and H.W. Rosenberg eds., TMS-AIME, Warrendale, PA, pp. 231-238, (1983).

[4] P.J. Bania and W.M. Parris, "BETA-21S: A High Temperature Metastable Beta Titanium Alloy", presented at the Titanium Development Association International Conference, Orlando, FL (1990).

[5] T.W. Duerig and J.C. Williams, "Overview: Microstructure and Properties of Beta Titanium Alloys", in Beta Titanium Alloys in the 80's, R.R. Boyer and H.W. Rosenberg, eds., TMS-AIME, Warrendale, PA, pp. 19-67, (1983).

[6] R.W. Schutz and D.E. Thomas, "Corrosion of Titanium and Titanium Alloys", in Metals Handbook, 9th edition, Vol. 13, ASM International, Metals Park, Ohio 44073, pp.669-706, (1987).

[7] A.D. McQuillan, "An Experimental and Thermodynamic Investigation of the Hydrogen-Titanium System", *Proceedings of the Royal Society of London*, Vol. A204, pp. 309-323 (1950).

[8] D.S. Shih, and H.K. Birnbaum, "Evidence of FCC Titanium Hydride Formation in β Titanium Alloy: An X-Ray Diffraction Study", *Scripta Met.*, Vol 20, pp 1261-1264, (1986).

[9] J.J. DeLuccia, "Electrolytic Hydrogen in Beta Titanium", Report No. NADC-76207-30, Naval Air Development Center, Warminster, PA 1976.

[10] J.S. Grauman, "A New High Strength, Corrosion Resistant Titanium Alloy", presented at the Titanium Development Association International Conference, Orlando, FL (1990).

[11] W.W. Gerberich, N.R. Moody, C.L. Jensen, C. Hayman, and K. Jatavallabhula, "Hydrogen in α/β and all β Titanium Systems", Hydrogen Effects in Metals, I.M. Bernstein and A.W. Thompson eds, TMS-AIME, Warrendale, PA, pp. 731-745 (1981).

[12] K. Nakasa and J. Liu, "Bending Strength of Hydrogen Charged Ti-13V-11Cr-3Al Alloy", K. Koshiya translator, *J. Japan Inst. Metals*, Vol. 55, No. 9, pp. 922-927, (1991).

[13] D.E. Thomas and S.R. Seagle, "Stress Corrosion Cracking Behavior of Ti-38-6-44 in Sour Gas Environments", Titanium Science and Technology, Vol. 4, G.Lutjering, U. Zwicker, and W. Bunk, eds., pp. 2533-2540, (1984).

[14] M.J. Blackburn and W.H. Smyrl, "Stress Corrosion and Hydrogen Embrittlement", Titanium Science and Technology, R.I. Jaffee and H.M. Burte, eds., New York, NY, pp. 2577-2609, (1973).

[15] H.G. Nelson, "Aqueous Chloride Stress Corrosion Cracking of Titanium - A Comparison with Environmental Hydrogen Embrittlement", Hydrogen in Metals, I.M. Bernstein and A.W. Thompson, eds., pp. 445-464, (1973).

[16] L.M. Young and R.P. Gangloff, "Hydrogen Environment Embrittlement of Beta Titanium Alloys", to be published in Proceedings of the Seventh World Conference on Titanium, F.H. Froes, ed., TMS-AIME, Warrendale, PA (1992).

[17] D.N. Fager and W.F. Spurr, "Some Characteristics of Aqueous stress Corrosion in Titanium Alloys", *Trans. ASM*, Vol. 61, (1968).

[18] R.P. Gangloff and J.R. Scully, "Mechanisms for the Environmental Cracking Resistance of High Strength Titanium Alloys", Proposal No. MS-DOD/ONR-4956-91, University of Virginia, Charlottesville, VA, (1991).

[19] N.E. Paton and O. Buck, in Effect of Hydrogen Behavior of Materials. I.M. Bernstein and A.W.Thompson, eds., TMS-AIME, Warrendale, PA, pp. 83-89, (1975).
[20] N.E. Paton, R.A. Spurling and C.G. Rhodes, in Hydrogen Effects in Metals, I.M.Bernstein and A.W. Thompson, eds., TMS-AIME, Warrendale, PA, pp. 269-279, (1981).
[21] J.E. Costa, D. Banerjee, and J.C. Williams, "Hydrogen Effects in β-Titanium Alloys", in Beta Titanium Alloys in the 80's, R.R. Boyer and H.W. Rosenberg, eds., TMS-AIME, Warrendale, PA, pp. 69-84, (1983).
[22] L.M. Young, Unpublished Research, The University of Virginia, (1992).
[23] C. Hayman and W.W. Gerberich, "X-ray Diffraction Studies of Titanium-Molybdenum Alloys", *Met. Trans.*, Vol 16A, February (1985).
[24] Y. Murakami, "Phase Transformation and Heat Treatment", Titanium 80 Science and Technology, H. Kimura and O. Izumi, eds., AIME, pp. 153-167, (1980).
[25] Z.A. Foroulis, "Factors Influencing Absorption of Hydrogen in Titanium from Aqueous Electrolytic Solutions", Titanium 80, Science and Technology, H. Kimura and O. Izumi eds., TMS-AIME, Kyoto, Japan, pp. 2705-2711 (1980).
[26] J. Liu and K. Nakasa, "Surface Peeling of Ti-6Al-4V Alloy Specimens during Hydrogen Charging", *J. Japan Inst. Metals*, Vol. 54, No. 11, pp. 1261-1269, (1990).
[27] J. S. Grauman, Personal Communication, 6 March 1992.
[28] P.W. Bridgman, Studies in Large Plastic Flow and Fracture, McGraw-Hill Book Company, Inc., New York, NY, (1952).
[29] J.W. Hancock and A.C. Mackenzie, "On the Mechanisms of Ductile Failure in High-Strength Steels Subjected to Multi-Axial Stress-States", *J.Mech. Phys. Solids*, Vol. 24, pp. 147-169, Pergamon Press, (1976).
[30] A.C. Mackenzie, J.W. Hancock, and D.K. Brown, "On the Influence of Stress on Ductile Failure Initiation in High Strength Steels", *Engineering Fracture Mechanics*, Vol. 9, pp. 167-188, (1977).
[31] W.R. Holman, R.W. Crawford, and F. Paredes, Jr., "Hydrogen Diffusion in a Beta Titanium Alloy", *Trans. AIME*, Vol. 22, pp. 1836-1939, (1965).
[32] P.N. Adler and R.L. Schulte, "Stress Induced Hydrogen Migration in β Phase Titanium", *Scripta Met.*, Vol. 12, pp. 669-672, (1978).
[33] N.E. Paton, O. Buck, and J.C. Williams, "The Effect of Hydrogen on the Strength, Modulus and Lattice Parameter of a Ti-Mo Alloy", *Scripta Met.*, Vol. 9, pp. 687-691, (1975).
[34] K. Nakasa, Personal Communication, 1 September 92.
[35] R. Lederich, McDonnell Douglas Corp., Personal Communication, September 1992.
[36] D.N. Williams, "The Hydrogen Embrittlement of Titanium Alloys", *J. Inst. Met.*, Vol. 91, pp. 147-152, (1962).
[37] R.S. Vitt and K. Ono, "Hydrogen Solubility in Alpha Titanium", *Met. Trans.*, Vol. 2, (1971).
[38] H. Margolin, "Stress, Hydrogen Segregation, and Fracture in α-β Titanium Alloys", *Met. Trans*, Vol. 7A, pp. 1233-1235, (1976).
[39] J.D. Boyd, "Precipitation of Hydrides in Titanium Alloys", *Trans. ASM*, pp. 977-988, (1969).

Table.1 Vendor reported and ingot chemistries in weight percent.

	Al	Nb	Si	Mo	Fe	C	H	O	N
Top	3.56	2.58	0.21	15.3	0.06	0.100	1.8	0.133	0.008
Bottom	2.86	2.41	0.27	14.5	0.08	0.011	---	0.138	0.005

Table 2. Summary of charging times and resulting hydrogen concentrations.

Charging Time	Total Hydrogen Concentration*	Comment
As-received	50-100 ppm	"Low Hydrogen"
24 Hours	950-1750 ppm	"Medium hydrogen"
64 Hours	1900-3600 ppm	"High Hydrogen"

*Total hydrogen was measure by vacuum hot extraction methods and includes mobile + trapped H.

Table 3. Fracture modes of a) near the edge and b) near the center of notched ß 21S (aged) tensile bars at room temperature.

a)

	Degree of Constraint		
Hydrogen Concentration (wt. ppm)	**0.52**	**0.62**	**1.03**
Low (50-100)	Microvoid Rupture	Microvoid Rupture	Microvoid Rupture*
Medium (950-1750)	Transgranular 2/ Intergranular	Transgranular 2/ Intergranular	Transgranular 2/ Intergranular
High (1900-3600)	Transgranular 2	Intergranular/ Transgranular 2	Intergranular/ Transgranular 2*

b)

	Degree of Constraint		
Hydrogen Concentration (wt. ppm)	**0.52**	**0.62**	**1.03**
Low (50-100)	Microvoid Rupture	Microvoid + Transgranular 1	Microvoid Rupture
Medium (950-1750)	Microvoid + Transgranular 1	Transgranular 1 + Microvoid	Transgranular 1*
High (1900-3600)	Transgranular 2*	Transgranular 1	Transgranular i

* Denotes case which is shown in Figure 6.

Figure 1. Optical Micrographs of TIMETAL 21S aged at 538 °C for a) 1hr and b) 8hrs. Polarized light, 30ml lactic acid, 10ml HNO_3, 5ml HF etchant.

a)

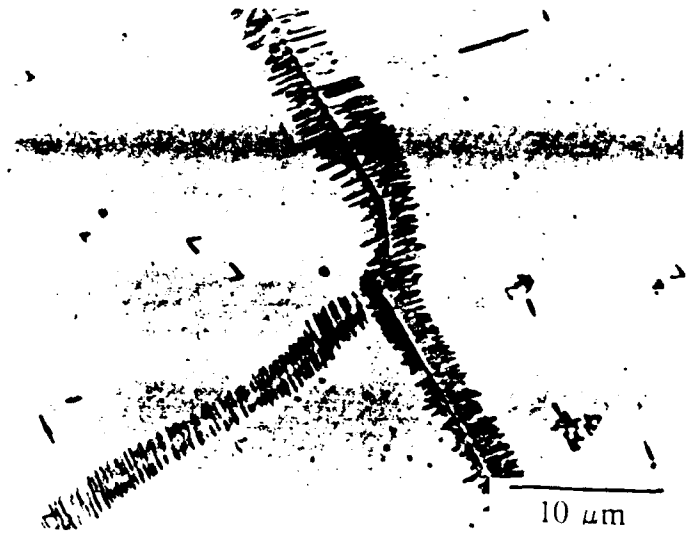

b)

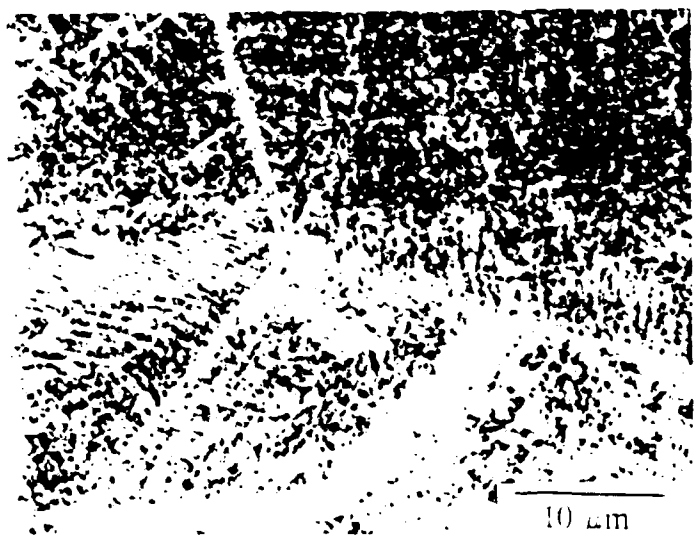

Figure 2. Diffraction patterns of a) solution annealed and b) peak aged TIMETAL 21S.

a)

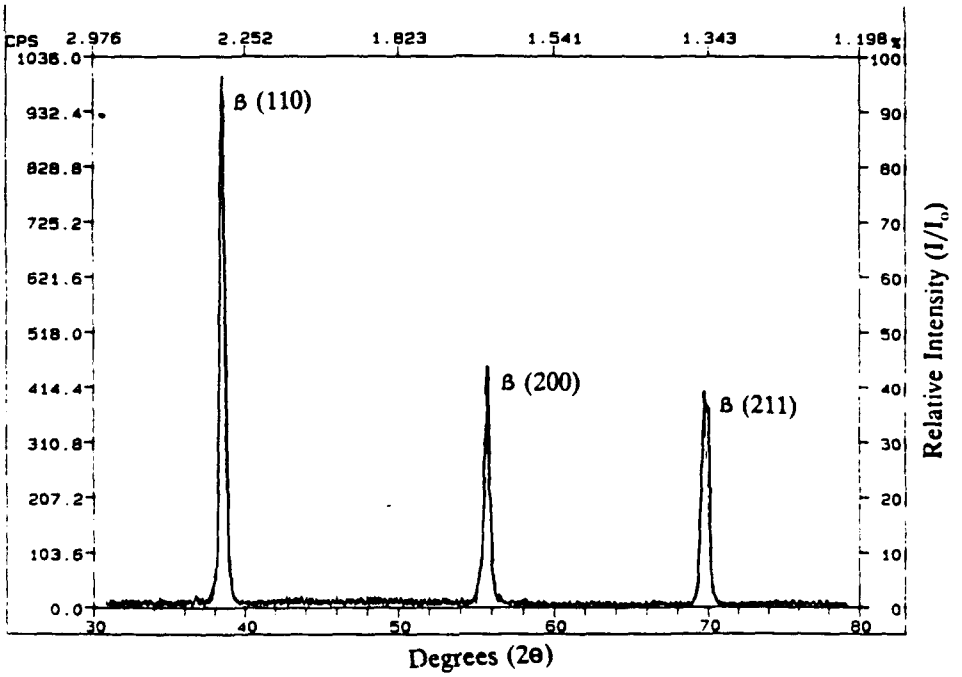

b)

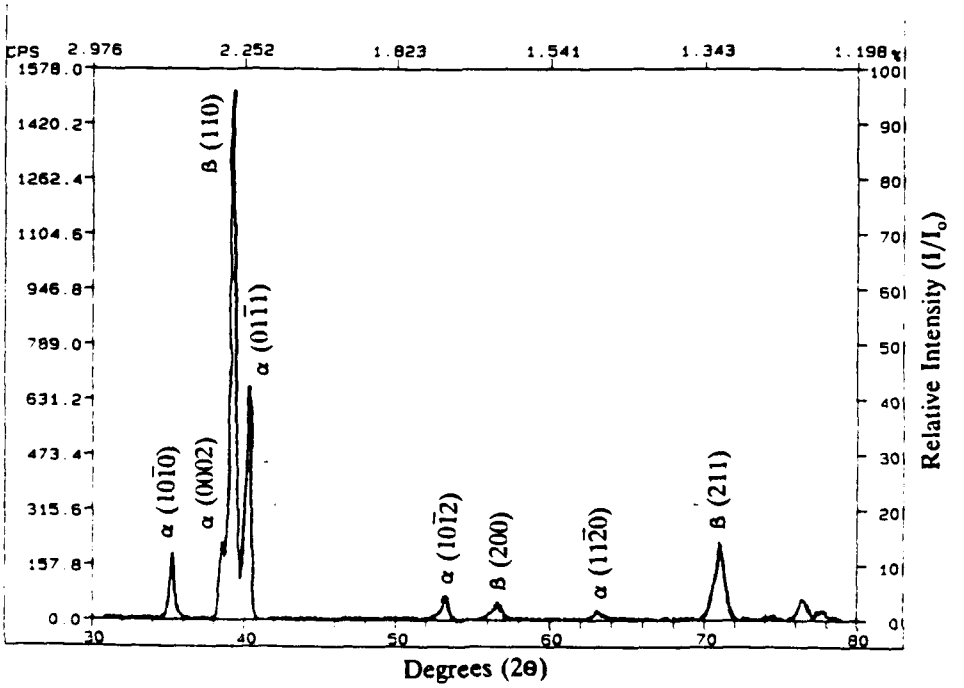

Figure 3. Schematic of the Electrochemical Charging Operation.

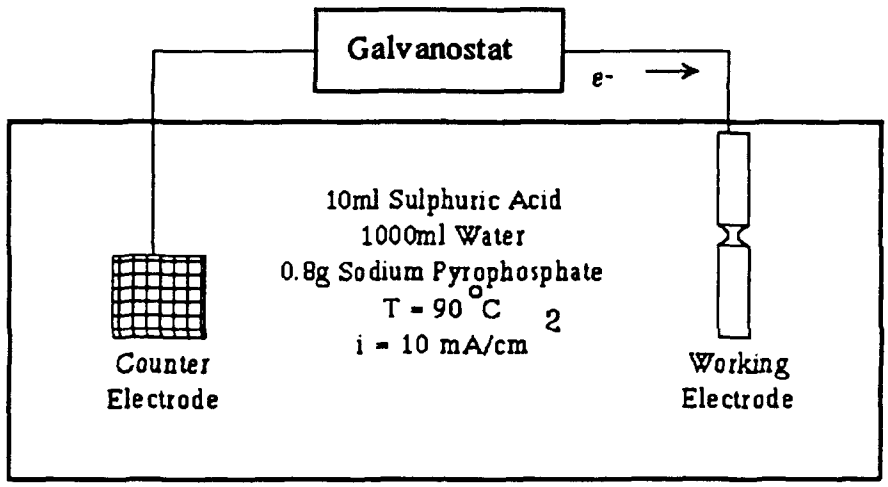

Figure 4. Bridgman equations describing the maximum longitudinal stress developed at the centerline of the tensile bar, the effective plastic strain across the notch diameter and the degree of triaxiality.

$$\sigma_Y = \sigma_F\left[1+\ln\left(\frac{D}{4R}+1\right)\right]$$

$$\epsilon^P = 2\ln\frac{D_0}{D}$$

$$\text{Degree of Triaxiality} = \frac{\sigma_m}{\sigma_F} = \frac{1}{3} + \ln\left(\frac{D_0}{4R} + 1\right)$$

σ_Y : *Maximum Longitudinal Stress at the Specimen Centerline*
σ_F : *Flow Stress*
ϵ^P : *Effective Plastic Strain Across the Notch Diameter*
D_O : *Initial Diameter Across the Notch*
D : *Instantaneous Diameter Across The Notch*
R : *Notch Radius*
σ_m : *Mean Stress*

Figure 5. Effect of hydrogen on the a) stress and b) strain developed at maximum load for aged ß 21S at room temperature.

a)

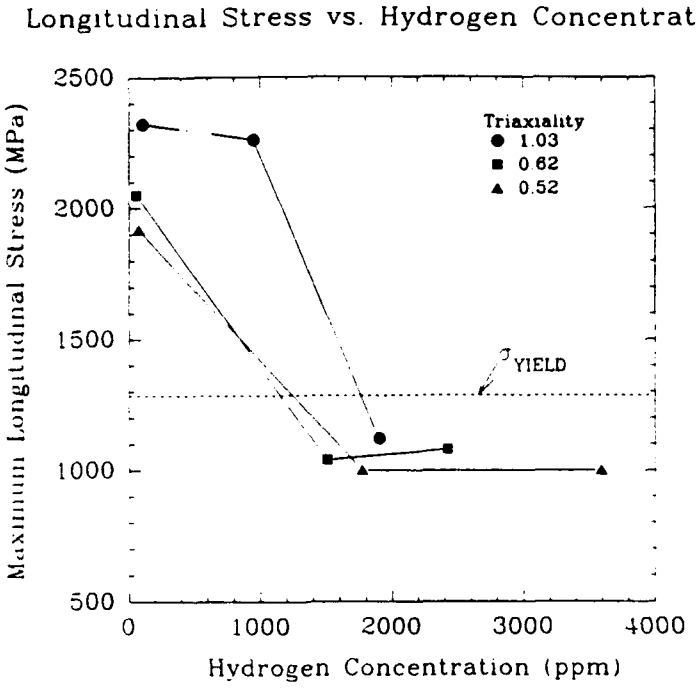

b)

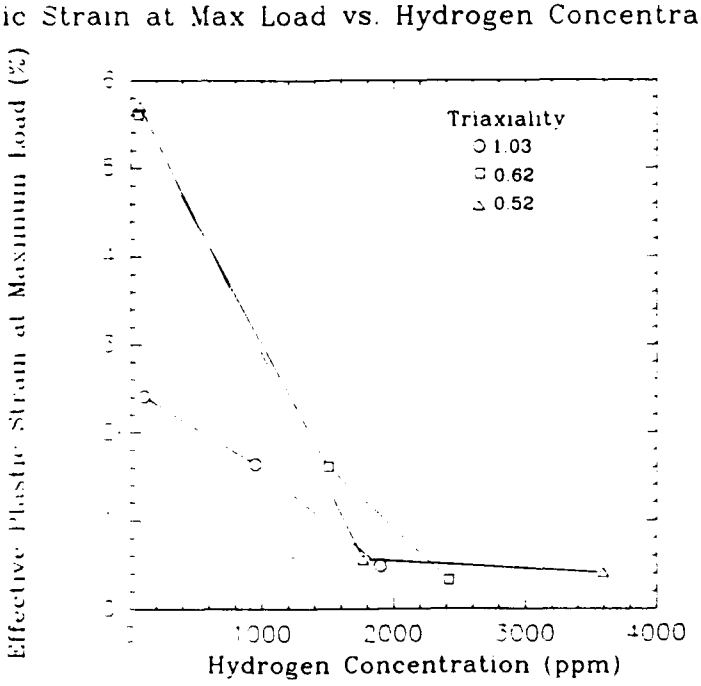

Figure 6. Fracture modes observed in peak aged TIMETAL 21S subjected to differing levels of hydrogen concentration and constraint. From top left clockwise, microvoid rupture, ductile tearing of α-β interfaces, transgranular fracture, intergranular fracture.

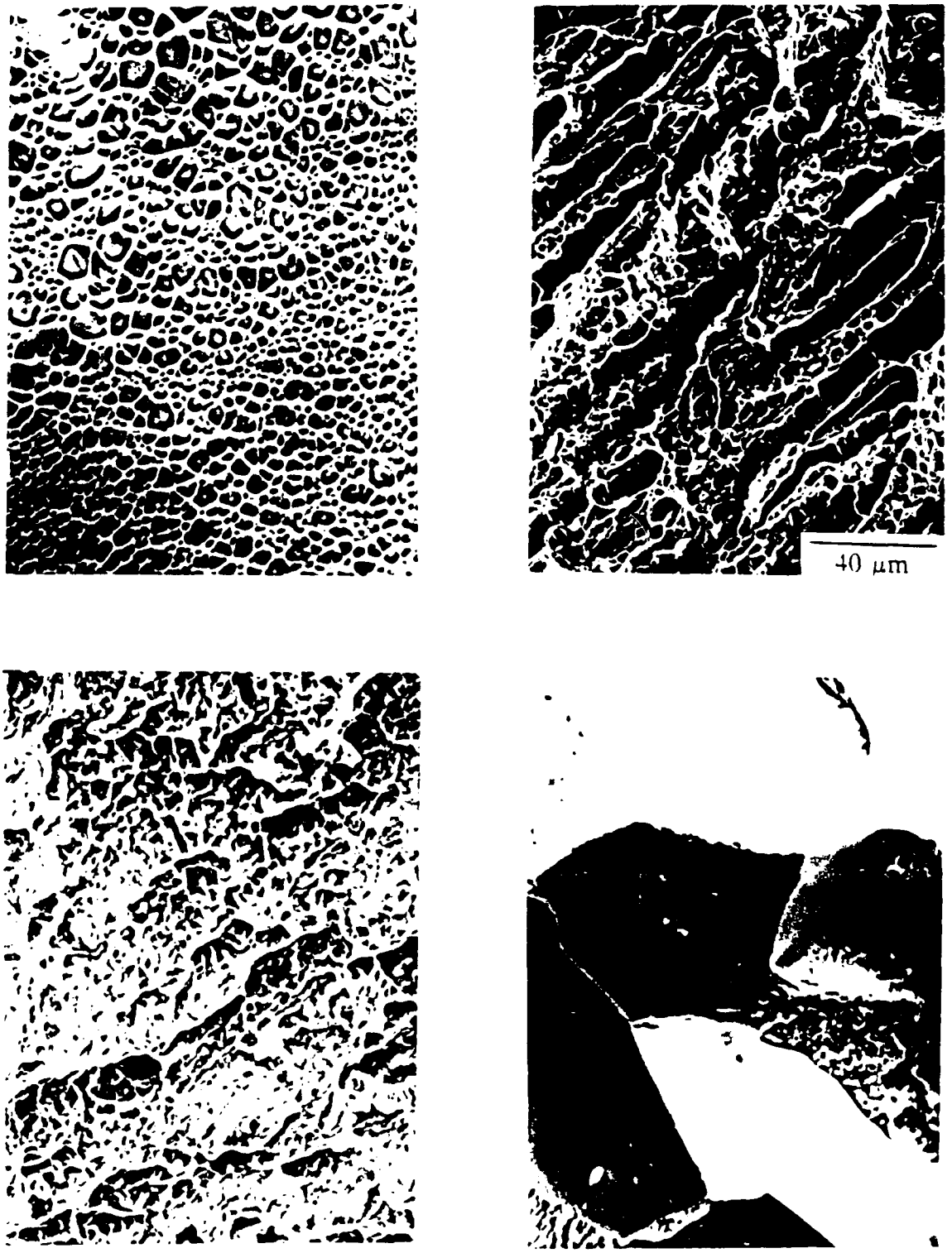

Figure 7. Diffraction spectra from a cross section of the high hydrogen, high constraint notch.

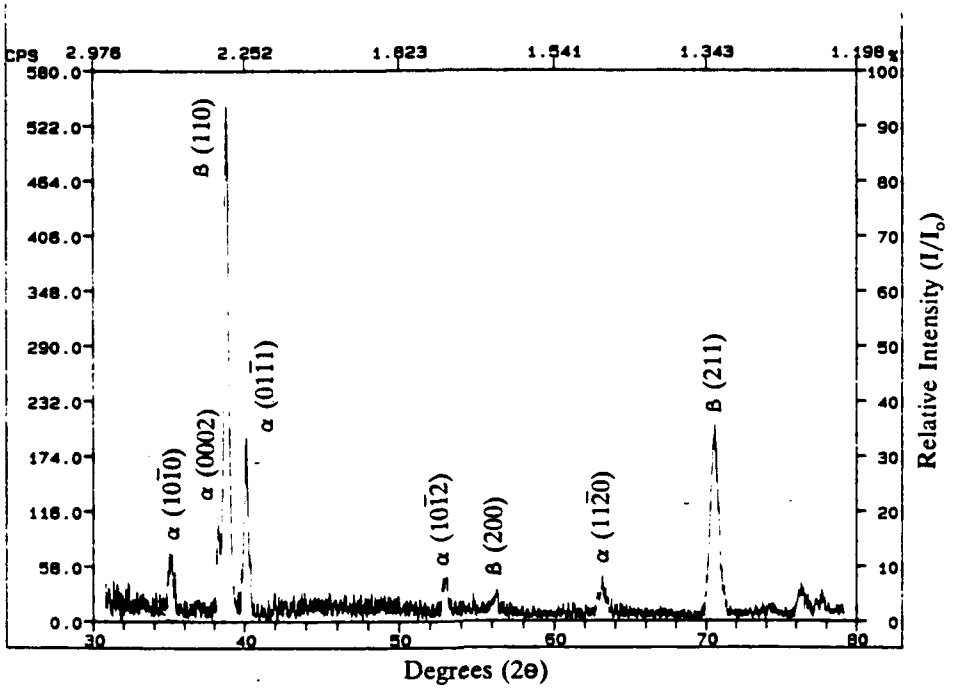

Figure 8a) Electron micrograph of surface damage in 64 hour charged TIMETAL 21S. Note that the size and morphology of the damaged region is similar to the α precipitate shown in Figure 1., suggesting the α has hydrided and spalled and b) diffraction spectra from the surface of a high hydrogen (64 hour charged) specimen.

a)

b)

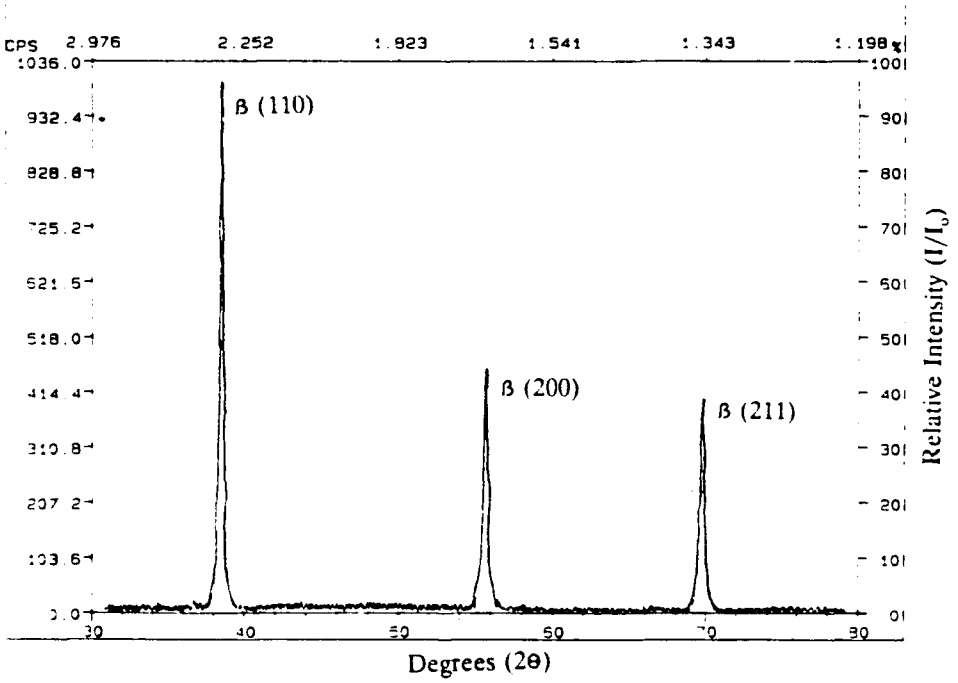

Figure 9. Diffraction spectra from a) δ hydride powder and b) hydrogen charged Grade 2 Ti.

a)

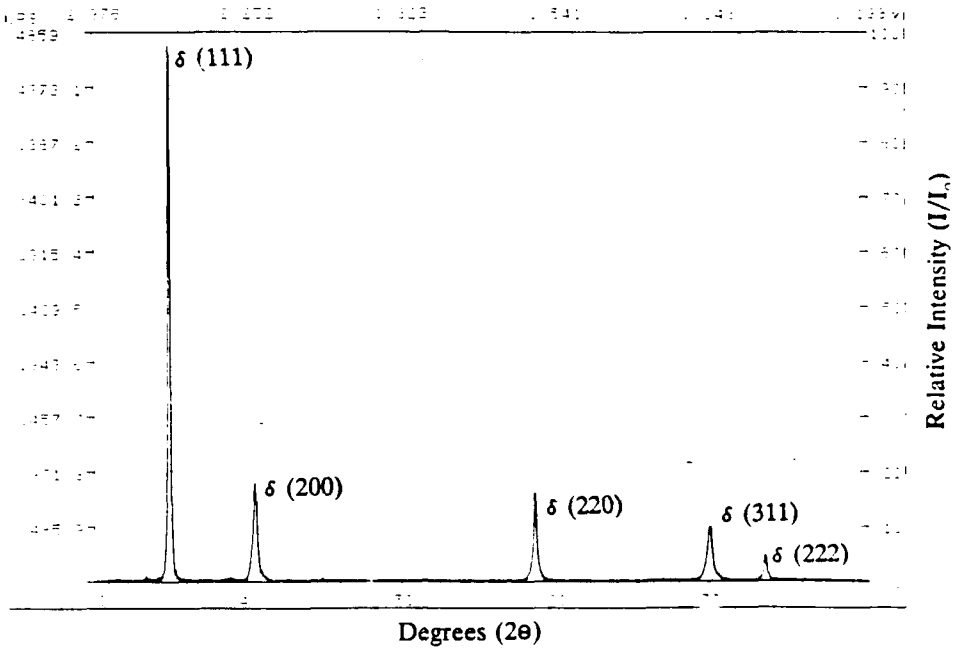

b)

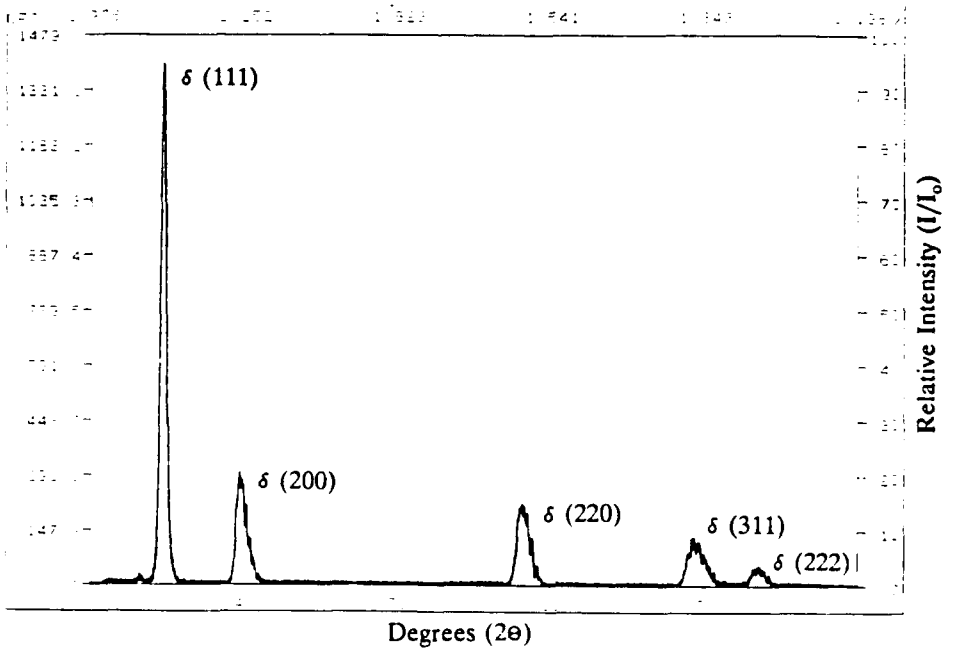

Figure 10. Comparison of a) hydrogen embrittled and b) aqueous EAC fracture morphology.

a)

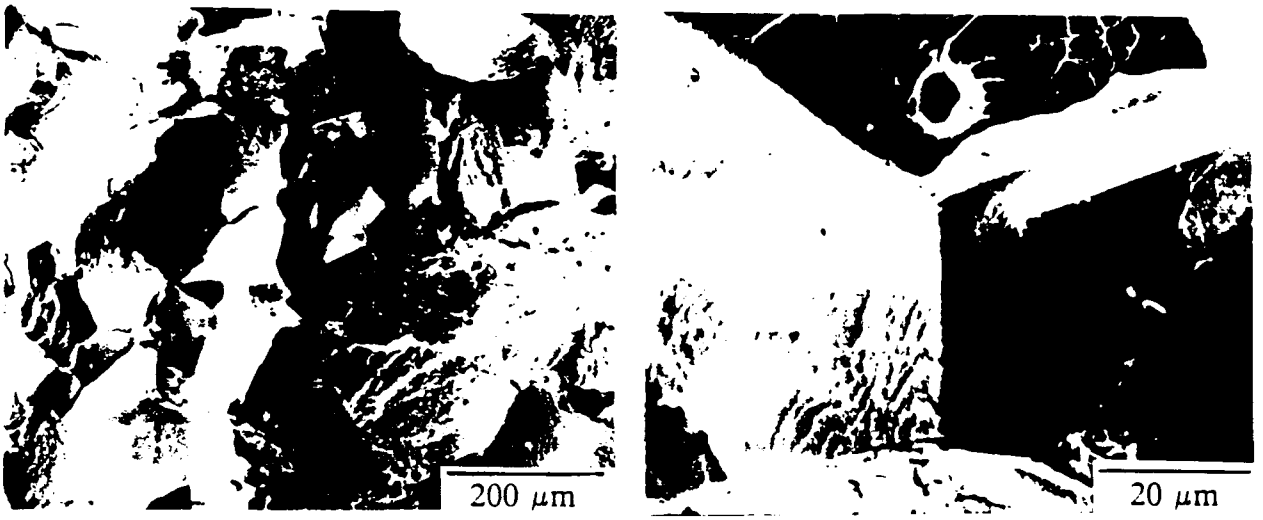

b)

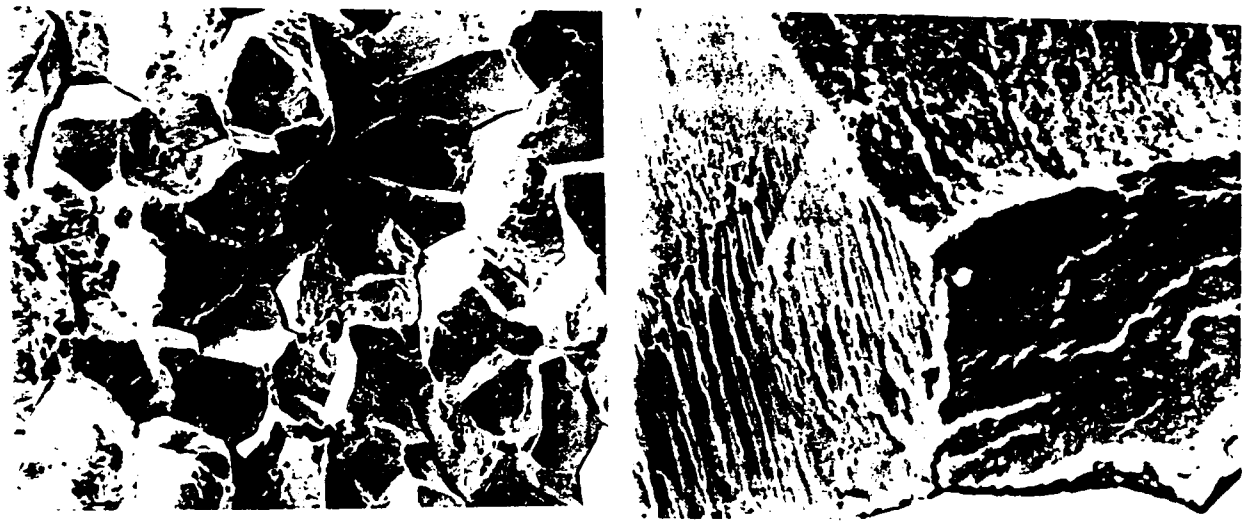

To be published in *Oxide Films on Metals & Alloys - Proceedings from the 182nd Meeting of the Electrochemical Society*, October, 1992.

CHARACTERIZATION OF THE PASSIVITY OF HIGH STRENGTH β-TITANIUM ALLOYS IN AMBIENT TEMPERATURE SOLUTIONS

D.G. Kolman and J.R. Scully

Center for Electrochemical Science and Engineering
Department of Materials Science
University of Virginia
Charlottesville, VA 22903

ABSTRACT

In an effort to understand the effect of Mo-Nb as well as V-Cr additions on the passivity of β-titanium alloys in ambient temperature solutions, characterization of the passive film on these alloys was undertaken. DC polarization, electrochemical impedance spectroscopy and ex-situ Auger electron spectroscopy techniques were utilized in order to compare peak aged (PA) and solution heat treated (SHT) samples of β-21S (Ti- 15Mo - 3Nb - 3Al) and Ti-15-3 (Ti - 15V - 3Cr - 3Sn - 3Al) to commercially pure titanium. It was found that there were no major electrochemical differences between the Mo-Nb stabilized alloy and the V-Cr stabilized alloy in both the PA and SHT conditions and that there were no "active" phases present in the PA alloys. The alloys examined were passive in all of the chloride solutions examined, including 5M HCl, and no significant effects of alloying additions on pitting potentials were observed. Cathodic polarization studies indicate similar exchange current densities for the hydrogen evolution reaction (HER) on all of the β-titanium materials. Because the exchange current density for the HER on Ti is less than that for the alloying additions, preliminary evidence suggests that the alloying additions are not incorporated into the oxide in amounts equal to that found in the alloys.

INTRODUCTION

β-titanium alloys are currently of interest for high strength applications in marine environments. They are attractive because of their low density and good general and localized corrosion resistance. However, one question regarding their seawater performance is their resistance to environmentally assisted cracking (EAC).

The EAC resistance of α-titanium alloys in seawater is known to be controlled by the tendency of the α phase to hydride[1,2]. In $\alpha + \beta$ alloys, the β phase has been shown to have a positive effect on the EAC resistance, plastically blunting cleavage cracks propagating through the hydrided α phase[3]. Little is known about the effects of α phase in a β-titanium matrix.

In contrast to α-titanium, a large hydrogen concentration (> 10,000 ppmw) is required for β-titanium alloys to hydride[4]. It is unclear whether such levels could be obtained in β-titanium alloys following a film rupture event in a marine environment. Thus, it is unknown whether or not a hydrogen mechanism is involved in the EAC behavior of these alloys or whether EAC is controlled by an entirely different mechanism such as slip - film rupture - dissolution or film induced cleavage[5]. In monotonic loading experiments on pre-cracked samples, EAC has been observed in PA β-21S[6]. It is plausible that mechanical destabilization of the passive film plays a role in either promoting dissolution or producing a means for hydrogen production and entry. These interrelated processes may occur following a film rupture event, leading to hydrogen production and absorption. Necessary stages include cation hydrolysis and resulting acidification which both destabilize the passive film and enhance hydrogen production or hydrogen production solely due to the large negative potential transient that occurs upon exposure of the bare titanium.

Two β-titanium alloys that are of particular interest are β-21S and Ti-15-3. Little is known about the electrochemical behavior of these alloys in marine environments. Therefore, as an initial step in elucidating the EAC mechanism, characterization of the passivity of these alloys has been undertaken. In order to obtain the required strength levels, these alloys are precipitation hardened through growth of an α precipitate with a needle-like morphology. Hence, a goal of this study is to examine the effect of microstructure on the electrochemical behavior of these alloys. Both solution heat treated and peak aged materials were investigated.

EXPERIMENTAL PROCEDURE

β-titanium samples were polished to a 600 grit finish followed by degreasing in acetone. The testing apparatus comprised 1 cm^2 area of the working electrode exposed in a flat cell containing a platinized niobium mesh counter electrode and a saturated calomel reference electrode (SCE) situated in a well possessing a Luggin capillary.

Polarization measurements were performed with either a PAR 173 or PAR 273 potentiostat at a scan rate of 0.05 mV/sec. All polarization experiments were performed following exposure to solution for two hours at open circuit.

Each electrochemical impedance spectroscopy (EIS) experiment comprised ten individual impedance scans. An initial scan was run at the open circuit potential followed by nine scans at 300 mV intervals from -0.3V to 2.1V vs. SCE. Each scan was preceded by a two hour potentiostatic hold at the given potential, except the open circuit potential scan which was preceded by two hours at open circuit. EIS measurements were performed with a Solartron 1286 electrochemical interface and a model 1255 frequency response analyzer. A 10 mV rms AC voltage signal was applied at frequencies between 100 kHz and 5 mHz using potentiostatic control. Impedance data fitting was performed with CNLS circuit fitting software[7].

β-21S was solution heat treated for 8 hours at 871°C (1600°F) followed by an air cool. Ti-15-3 was solution heat treated for 30 minutes at 816°C (1500°F) followed by an air cool. Peak aging of both alloys comprised subsequent single step heat treatment at 538°C (1000°F) for 8 hours followed by an air cool. Commercially pure grade 2 Ti (α phase) was also examined as a "control" alloy. Further, Mo, Nb, V, and Cr are known to be β phase stabilizers, while Al and Sn are known to be α stabilizers. Therefore, grade 6 Ti (Ti - 5 Al - 2.5 Sn) was utilized in order to simulate the behavior of the α precipitates found in the β-titanium alloys.

Electrochemical tests performed on the materials utilized five different room temperature solutions - aerated and deaerated 0.6M NaCl, aerated and deaerated 0.6M NaCl adjusted to pH 1 with HCl, and aerated 5M HCl. 0.6M NaCl solutions comprised reagent grade NaCl added to distilled deionized water. A second set of solutions was adjusted to pH 1 with reagent grade HCl. 5M HCl solutions comprised reagent grade HCl and distilled deionized water. The pH of these solutions is calculated to be -1.64 when the effect of Cl^- on the activity of H^+ is incorporated into the calculation. Deaeration was performed with commercially pure Ar gas. 0.6M NaCl was utilized in order to model alloy behavior when exposed to the bulk solution in a marine environment. The pH 1 0.6M NaCl was utilized in order to discern the behavior of the alloys in a simulated crack tip environment. Although a crack tip solution has yet to be isolated, a pH 1 0.6M NaCl is considered a rough estimate of that solution. Aerated 5M HCl was utilized in order to analyze material behavior under extremely acidic conditions that are perhaps more severe than a crack tip environment. Gravimetric tests were performed in 9.09 vol% HF at 85°C utilizing reagent grade HF and distilled deionized water.

RESULTS AND DISCUSSION

pH 1 0.6M NaCl Solutions

Representative anodic polarization data are reported in Figures 1 and 2.

Figure 1 shows the anodic polarization behavior of the six different materials (SHT & PA β-21S, SHT and PA Ti-15-3, grade 2, and grade 6) in a particular solution. Figure 2 reveals the behavior of one particular material in the five solutions (aerated and deaerated 0.6M NaCl, aerated and deaerated pH 1 0.6M NaCl, and aerated 5M HCl). It may be seen in Figure 1 that a rapid increase in anodic current density is observed for each material at approximately 1.4V. This rapid increase in anodic current density corresponds to the onset of oxygen evolution and is not due to pitting. This has been confirmed by optical microscopy. Additionally, Figure 1 reveals that SHT β-21S has the highest passive current density of all of the materials. This was found to be true in all of the solutions examined. In contrast, the magnitudes of the passive current densities of the other materials varied between solutions and were probably within experimental error.

Figure 1 additionally reveals that the open circuit potentials for all of the materials are within experimental variability (150mV) for one material. Grade 6 Ti, which loosely models the α precipitates in the peak aged materials, has a similar open circuit potential to that of the SHT materials. This indicates that no significant galvanic cells are present between the β-titanium matrix and the α precipitates in the PA materials. Further, no increases in anodic current density are observed at potentials corresponding to the oxidation of alloying additions.

Figure 2 displays the polarization curves for SHT β-21S in the five solutions. It may be seen that as the pH decreases, the passive current density increases, as would be expected. It also may be seen that all of the materials were passive with no observed pitting potential. Additionally, the potential at which the rapid increase in anodic current density occurs increases with increasing H^+ content, as predicted by the thermodynamic relationship between the redox potential and pH. This further confirms the hypothesis that this current density increase is indeed due to oxygen evolution and not due to the onset of pitting. Further, no differences are observed between the aerated and deaerated conditions. This has been observed previously by others in abrasion experiments[8].

EIS is a useful method for characterizing the passivity of materials in-situ. A proposed circuit model for the electrochemical interface may be seen in Figure 3. This model includes C_{ox} which represents the space charge capacitance of a compact non-porous oxide. The model also comprises a double layer capacitance (C_{dl}) at the oxide/solution interface. Constant phase elements are used to better represent the non-idealities of such capacitances.

An example of the obtained impedance data may be seen in Figures 4a and b, which show the impedance response of SHT Ti-15-3 in aerated pH 1 0.6M NaCl. It is seen that as the potential is increased, the low frequency impedance decreases. Further, as the potential is increased away from open circuit, the emergence of two

time constants is seen. This occurs until 1.8V is reached, wherein the two time constants merge again. At these potentials, deconvolution of the data becomes increasingly difficult. However, it is seen that the impedance response is adequately accounted for by the proposed circuit model. Good correlation was obtained between the model and the experimental data as seen in Figure 5.

It was hypothesized that the high frequency time constant was attributable to the oxide and that the low frequency time constant was attributable to the parallel R_{ct}/C_{dl} combination. In order to confirm this hypothesis, ellipsometric data for titanium oxide thickness at various potentials in 0.1M HCl was reported in the literature[6]. Impedance spectra for grade 2 Ti were then obtained at 0V, 2V, 4V, 6V, and 8V vs. NHE, with the specimen prepared in identical fashion to those of the ellipsometric study. Utilizing a dielectric constant of 100 for TiO_2, a good correspondence between the literature and experiment was obtained for the oxide thickness, as seen in Figure 6. This confirms the hypothesis that the high frequency time constant was indeed attributable to the oxide.

Example plots of the interfacial parameters obtained by fitting vs. potential may be seen in Figures 7a and b. The charge transfer resistance for grade 2 Ti in aerated pH 1 0.6M NaCl increases with potential until approximately 1.2V whereupon the charge transfer resistance begins to decrease. The decrease in the charge transfer resistance coincides with the onset of oxygen evolution, as discussed earlier. The oxide capacitance is found to decrease with increasing potential. This is expected, because the oxide thickness, which is inversely proportional to the capacitance, is known to increase with increasing potential for titanium[9]. The oxide resistance displays no real trend with potential, however this is to be expected as the oxide resistance is comprised of the oxide resistivity which decreases with increasing potential and the oxide thickness which increases with increasing potential.

Oxide thickness and resistivity were calculated from the parameters obtained by circuit fitting. The oxide thickness may be calculated by utilizing the equation

$$d_{ox} = \frac{\varepsilon \varepsilon_o A}{C_{ox}} \qquad (1)$$

where d_{ox} is the oxide thickness, C_{ox} is the oxide capacitance, ε is the dielectric constant of the oxide, ε_o is the permittivity of free space, and A is the surface area. The oxide resistivity may be calculated as follows, assuming that it varies linearly with thickness. From equation 1,

$$\frac{A}{d_{ox}} = \frac{C_{ox}}{\varepsilon \varepsilon_o} \qquad (2)$$

It is known that

$$\rho_{ox} = R_{ox}\left(\frac{A}{d_{ox}}\right) \tag{3}$$

Therefore, substituting (2) into (3), the equation

$$\rho_{ox} = \frac{R_{ox} C_{ox}}{\varepsilon \varepsilon_o} \tag{4}$$

is obtained.

Figure 7c shows a plot of the oxide thickness and resistivity vs. potential for grade 2 Ti in aerated pH 1 solution. It is seen that the oxide thickness increases linearly with increasing potential (approximately 23Å/V). This corresponds with earlier observations for commercially pure titanium in 0.1M HCl[9]. Additionally, it can be seen that the oxide resistivity decreases with potential, implying that the oxide is becomingly increasingly defective. It should be noted that handbook values for bulk TiO_2 are listed[10] as being the range of 10^{13} - 10^{18} ohms-cm, while calculated values from experiment yield values in the 10^7 - 10^{10} range, depending upon potential. This discrepancy may be due to the fact that a thin oxide in solution is more defective than the bulk oxide, the oxide incorporates alloying additions, or both. In deaerated pH 1 0.6M NaCl solutions, the oxide growth rate was found to be much smaller, approximately 5.4Å/V.

Absolute values for oxide thickness and resistivities can only be calculated for materials with known dielectric constants. The dielectric constants for both β-21S and Ti-15-3 are unknown. Therefore, no thicknesses or resistivities are reported here. However, by independently obtaining the oxide thickness through Auger electron spectroscopy, a dielectric constant may be subsequently calculated for these materials. This is an object of future study.

Although the six materials behaved differently in various solutions, some overall trends may be observed. The charge transfer resistance associated with passive dissolution is approximately an order of magnitude larger than the oxide resistance. Therefore, the passive dissolution will be dominated by the charge transfer reaction and not by charge passage across the oxide. Other findings include that fact that the charge transfer resistance decreases as the solution pH decreases, coincident with an increase in the passive current density. Still further, the charge transfer resistance has been found to be smaller for Ti-15-3 than β-21S. This is curious because the passive current density for Ti-15-3 was found to be lower than that for β-21S in many cases from DC experiments. This indicates that there is a change in charge transfer mechanism associated with passive dissolution between the two alloys, although the exact change in mechanism is unclear.

Preliminary Auger electron spectroscopy (AES) data obtained from SHT samples of Ti-15-3 exposed to aerated pH 1 0.6M NaCl indicate that there is little or no V and Cr in the outer regions of the oxide. AES data obtained from SHT β-21S in the identical solution were inconclusive. Although these studies are preliminary, it may tentatively be hypothesized that the oxides on β-titanium alloys stabilized with either Mo and Nb or with V and Cr contain few alloying additions in the passive film. This is supported by the similar passive electrochemical behaviors observed in various solutions. Others have observed similar results on α, α/β, and β-titanium alloys[11].

0.6M NaCl Solutions

The behavior of the titanium alloys in neutral 0.6M NaCl was found to be nearly identical to that observed in pH 1 adjusted solutions. The passive current densities for all of the materials were lower in the neutral solution than in pH 1. This was confirmed by impedance measurements wherein the charge transfer resistances which dominate the polarization resistance and hence the passive current density were found to be higher. Additionally, the oxide resistances appeared to be higher for the neutral solutions due to both increased oxide resistivity and increased oxide thickness.

As in the pH 1 solutions, there appeared to be no discernible difference between aerated and deaerated conditions. Furthermore, there appeared to be no significant differences between the oxides on the β-titanium alloys stabilized with Mo and Nb and those stabilized with V and Cr. However, as in the pH 1 solutions, SHT β-21S displayed the highest passive current density of all of the materials examined. The open circuit potentials, including grade 6 Ti, all were within experimental variability, again indicating that no significant galvanic couples are present in the PA materials.

Cathodic polarization scans performed in deaerated 0.6M NaCl indicated similar exchange current densities for the hydrogen evolution reaction (HER) on all of the β-titanium materials, ranging from 2×10^{-11} to 4.6×10^{-11} A/cm^2. Although these were found to be higher than that found for grade 2 Ti (1×10^{-12} A/cm^2), the exchange current densities are far below those found for the HER on the individual alloying additions. In combination with the AES results and the fact that no increases in the anodic current density corresponding to oxidation of alloying additions were observed, it may be hypothesized that there are few alloying additions incorporated into the oxides of the β-titanium materials.

Aerated 5M HCl

All of the materials examined were passive in all of the chloride solutions

examined, including 5M HCl, with no pitting potential observed. The passive current densities for all of the materials were highest in the aerated 5M HCl, as would be expected due to its low pH. No significant differences were observed in the passive electrochemical behavior between the Mo-Nb and V-Cr stabilized materials although SHT β-21S again displayed the highest passive current density of all of the materials.

It may be seen from Figure 2 that the oxygen evolution reaction ceases at 2.2V. It is hypothesized that this is due to increased difficulty in electron tunneling through the semiconducting passive film which thickens with increasing potential. This phenomenon was observed in all solutions and on all materials, albeit at different potentials. Additionally, the computed oxide growth rate for grade 2 Ti was found to be 16Å/V.

It should be noted that the measured passive current densities for the materials in 5M HCl, the most aggressive solution examined, are five orders of magnitude too low to solely account for crack growth rates observed[6]. Therefore, it may be concluded that highly localized mechanical destabilization of the passive film is required for EAC of these alloys, regardless of the exact mechanism.

Good correlation between the proposed circuit model and data was observed for all of the materials in all of the solutions except 5M HCl. Figure 8 displays the impedance response of PA β-21S in aerated 5M HCl at five different potentials. It may be seen that additional time constants (i.e. low frequency inductive looping) are present in the spectra that are not seen in any of the spectra from other solutions. The origin of this looping is unclear but it appears to indicate a change in the properties of the electrochemical interface.

Hot HF Solutions

Gravimetric analysis of PA β-21S and Ti-15-3 in 9.09 vol% HF at 85°C was performed in order to examine the effects of alloying additions on the dissolution of the alloys. Two sets of experiments were performed. The first set involved cathodic polarization at 0.13mA/cm^2. β-21S, stabilized with Mo and Nb, was found to have a penetration rate of 5 mils/hr. which was half of that found for the V and Cr stabilized alloy. Additionally, hydrogen concentrations were found to be higher in the V-Cr stabilized Ti-15-3 (622ppm) than in the alloy containing Mo and Nb (409 ppm). A second set of experiments was then performed at open circuit. The penetration rate was again found to be higher in the PA Ti-15-3 (110 mils/hr.) than in the PA β-21S (90 mils/hr.). Therefore, it may be concluded that Ti-15-3 has a higher corrosion rate and hydrogen uptake in this solution.

CONCLUSIONS

Analysis of the passive film on β-titanium alloys in room temperature solutions simulating crack tip chemistries possible in marine environments has been performed utilizing both DC and AC methods. It was found that there are no major electrochemical differences between Mo and Nb stabilized β-21S and V and Cr stabilized Ti-15-3 in their PA and SHT forms, although SHT β-21S consistently yielded the largest passive current density in all chloride solutions. Moreover, there do not appear to be any significant differences between either the model precipitate (grade 6 Ti) or commercially pure Ti (grade 2 Ti) and the β-titanium alloys. This finding suggests that there is minimal galvanic interaction in PA materials. No pitting potential was observed in these alloys in any chloride containing solution including 5M HCl. EIS experiments conducted with 5M HCl indicated that a simple two time constant circuit model was not applicable to those experiments. Furthermore, all of the alloys in this study were found to be passive in all of the solutions except hot HF and yielded passive current densities that were at least five orders of magnitude too low solely to account for crack growth rates observed. The passive film, therefore, must be destabilized in order to account for these crack growth rates. Further, alloy dissolution was found to be controlled by the charge transfer reaction. The mechanism of this reaction appears to be different on the different β-titanium alloys. Hydrogen evolution kinetics, the lack of observed alloying addition oxidation, and preliminary AES studies tentatively indicate little incorporation of alloying additions into the passive film. Further, experiments in hot HF indicated that the V-Cr stabilized alloy had a higher corrosion rate and hydrogen uptake than the Mo-Nb stabilized alloy.

ACKNOWLEDGEMENTS

The authors would like to acknowledge the Office of Naval Research (Grant N00014-91-J-4164) and the Virginia Center for Innovative Technology for their support of this work. The authors would also like to thank Titanium Metals Corporation for their generous donation of alloys and George Young for his work with Ti exposed to HF solution.

REFERENCES

1) D.N. Williams, *J. Inst. of Metals*, Vol. 91, pp. 147-152 (1962-63).

2) H.G. Nelson, in *First Thermal Structures Conference*, E. Thornton ed., University of Virginia, Charlottesville, VA, pp. 301-311 (1990).

3) D.N. Fager and W.F. Spurr, *Trans. ASM*, Vol. 61, pp. 283-292 (1968).

4) A.D. McQuillan, *Proc. Roy. Soc.*, Vol A204, p. 309 (1950).

5) T.R. Beck, *Corrosion*, Vol. 30, pp. 408-414 (1974).

6) L.M. Young and R.P. Gangloff, "Proceedings, Seventh World Conference on Titanium", S.H. Froes ed., TMS-AIME, Warrendale, PA, in publication.

7) J.R. MacDonald, "Complex Nonlinear Least Squares Immitance Fitting Program", University of North Carolina, Chapel Hill, NC, Version 3.02.

8) K. Vetter, "Electrochemical Kinetics", p. 767, Academic Press, New York (1967).

9) T. Oshtsuka, M. Masuda, N. Sato, *J. Electrochem. Soc.*, Vol. 132, pp. 787-792 (1985).

10) "Handbook of Chemistry and Physics", R.C. Weast ed., 64th edition, Chemical Rubber Publishing Co., Boca Raton, FL, p. E-55 (1983-4).

11) P.A. Mäusli, S.G. Steinemann, and J.P. Simpson, "Proceedings of the Sixth World Conference on Titanium", P. Lacombe, R. Tricot and G. Béranger, eds., pp. 1759-1764 (1988).

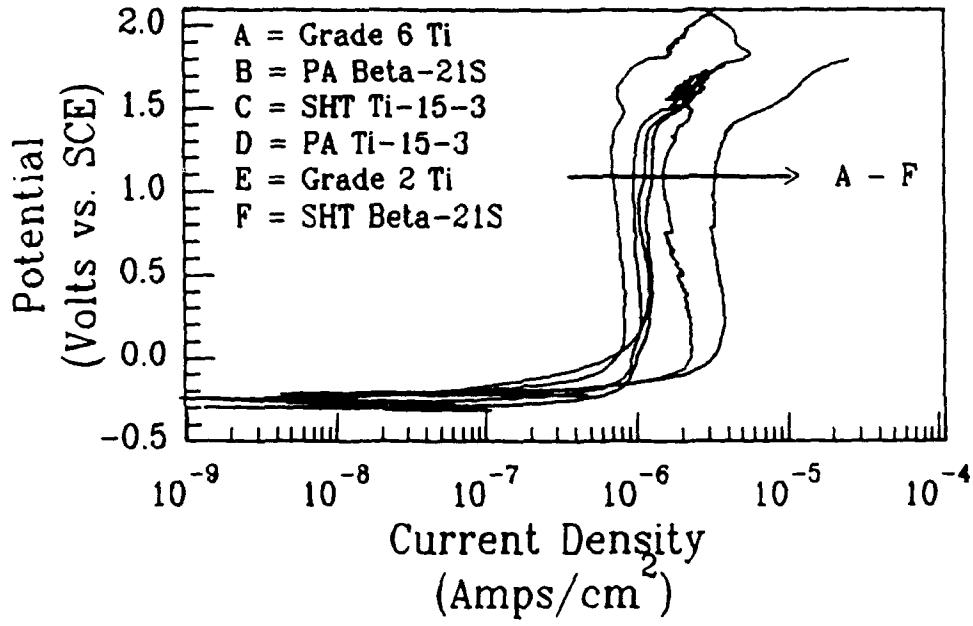

Figure 1 - Representative anodic polarization scans for the six materials examined in one particular solution (aerated pH 1 0.6M NaCl).

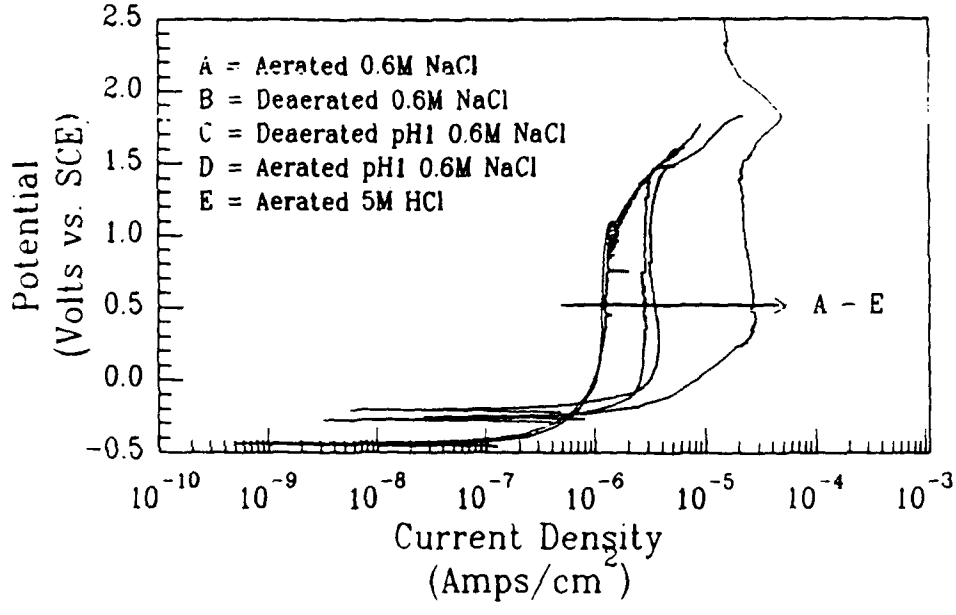

Figure 2 - Representative anodic polarization scans for one particular material (SHT β-21S) in the five solutions examined.

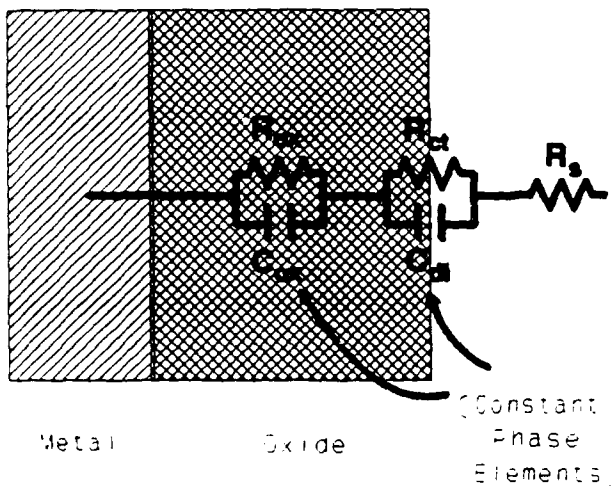

Figure 3 - Proposed circuit model for titanium samples exposed to solution.

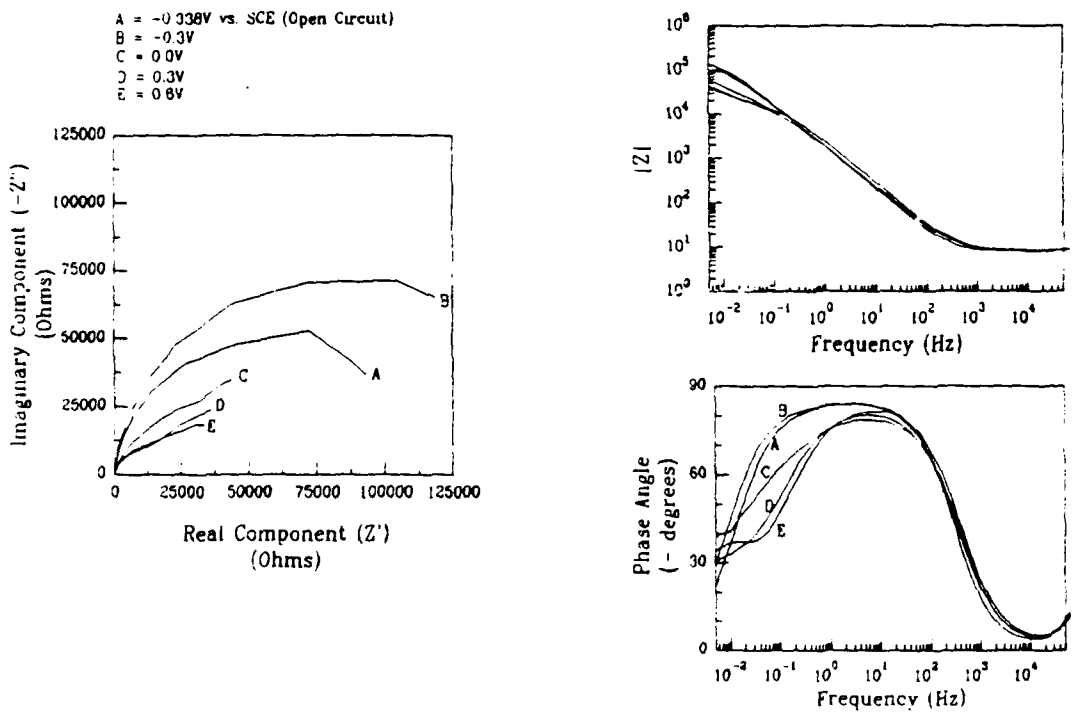

Figure 4a - Representative electrochemical impedance response of a titanium sample (SHT Ti-15-3 exposed to aerated pH 1 0.6M NaCl) at potentials ranging from open circuit to 0.6V vs. SCE.

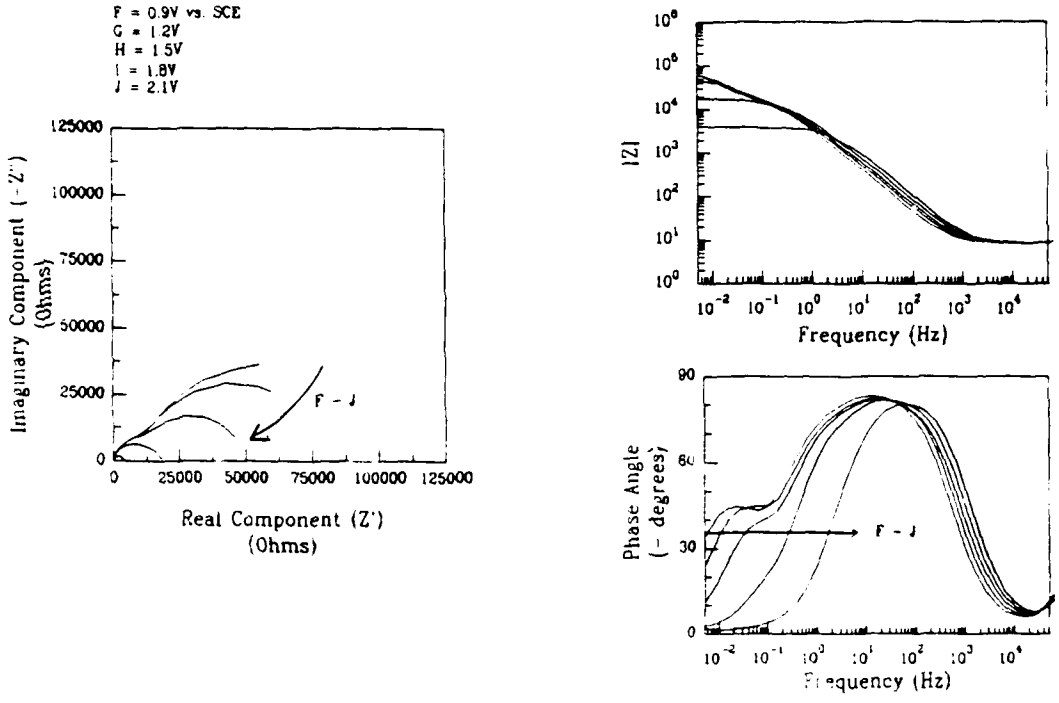

Figure 4b - Representative electrochemical impedance response of a titanium sample (SHT Ti-15-3 exposed to aerated pH 1 0.6M NaCl) at potentials ranging from 0.9V to 2.1V vs. SCE.

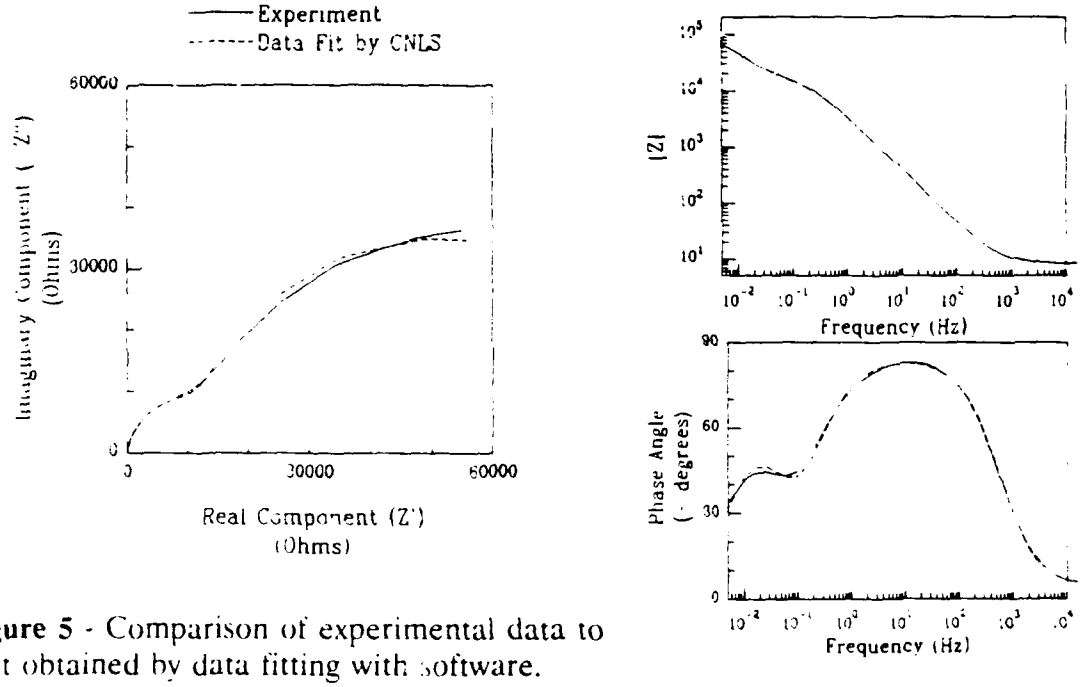

Figure 5 - Comparison of experimental data to that obtained by data fitting with software.

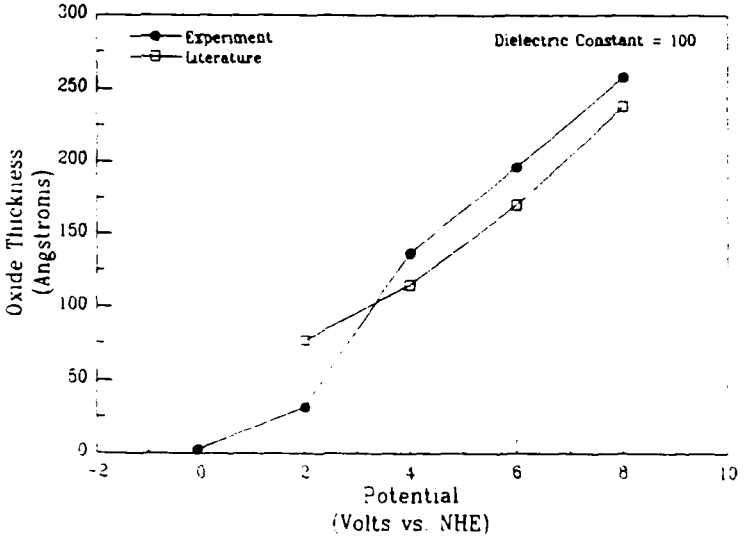

Figure 6 - Comprison of oxide thicknesses on grade 2 Ti in 0.1M HCL vs. that reported in the literature[9].

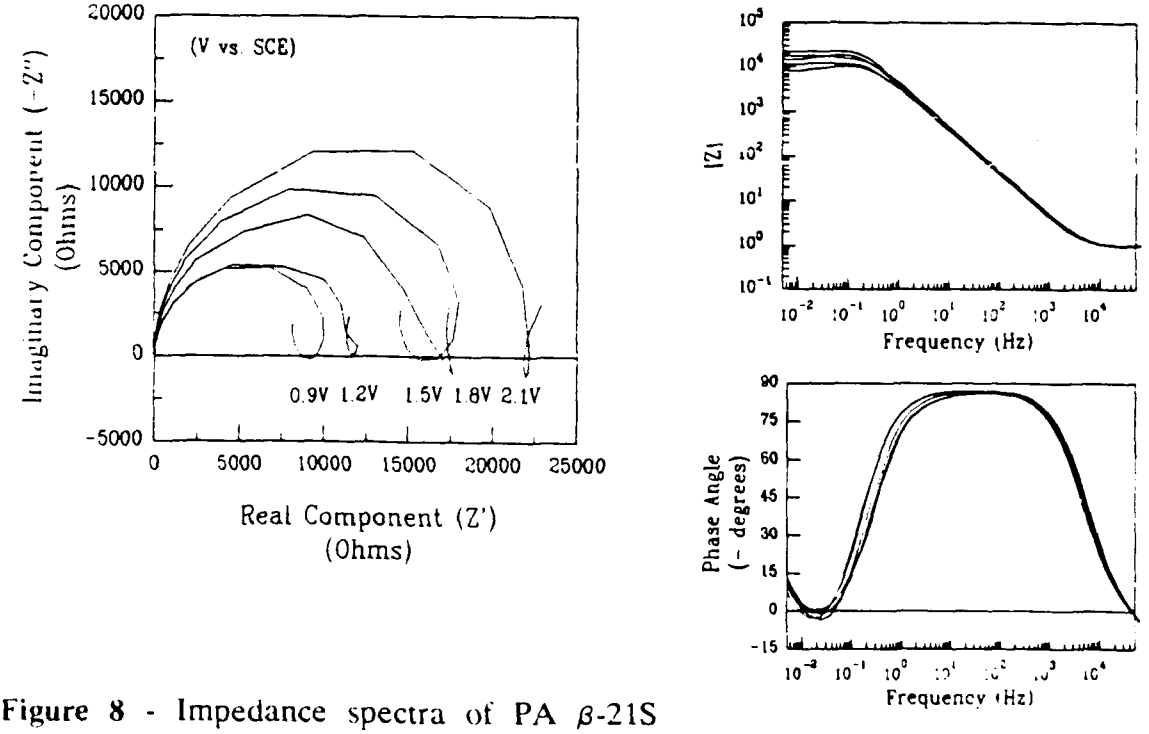

Figure 8 - Impedance spectra of PA β-21S exposed to aerated 5M HCl.

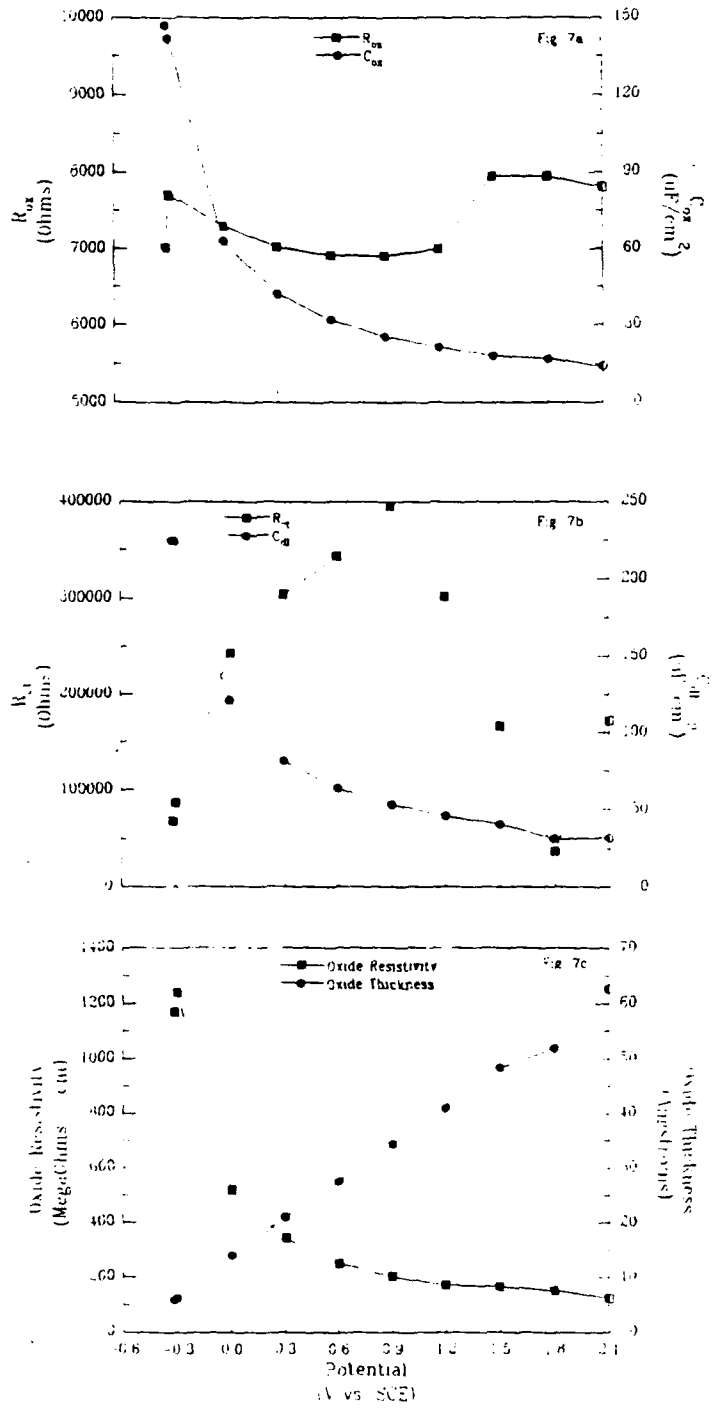

Figure 7 - Plots of parameters obtained through data fitting vs. potential for grade 2 Ti exposed to aerated pH 1 0.6M NaCl.

DISTRIBUTION LIST

1 - 3 Dr. A. John Sedriks
Materials Division, Code 1131
Office of Naval Research
800 N. Quincy Street
Arlington, VA 22217-5000

4 - 6 Director
Naval Research Laboratory
Washington, DC 20375
Attention: Code 6000
Code 6300
Code 2627

8 - 18 Defense Technical Information Center, S47031
Building 5, Cameron Station
Alexandria, VA 22314

19 Ms. Charlotte Luedeke
Administrative Contracting Officer
Office of Naval Research
Resident Representative
2135 Wisconsin Avenue, N. W.
Suite 102
Washington, DC 20007

20 - 21 E. H. Pancake, Clark Hall, UVA

22 Naval Air Development Center
Code 606
Warminster, PA 18974
Attention: Dr. J. DeLuccia

23 - 24 Commanding Officer
Naval Surface Warfare Center
Silver Spring, MD 20903-5000
Attention: Library Code
Code R33

25 Naval Ocean Systems Center
San Diego, CA 92152-5000
Attention: Library

26 Naval Postgraduate School
Monterey, CA 93940
Attention: Mechanical Engineering Dept.

27 - 29 Naval Air Systems Command
Washington, DC 20360
Attention: Code 310A
Code 5304B
Code 931A

30 - 31 Naval Sea Systems Command
Washington, DC 20362
Attention: Code 05M
Code 05R

32 Naval Civil Engineering Laboratory
Port Hueneme, CA 94043
Attention: Materials Division

33 Naval Electronics Laboratory
San Diego, CA 92152
Attention: Electronic Materials
Sciences Division

34 Commander
David Taylor Research Center
Bethesda, MD 20084

35 Naval Underwater Systems Center
Newport, RI 02840
Attention: Library

36 Naval Weapons Center
China Lake, CA 93555
Attention: Library

37 NASA
Lewis Research Center
21000 Brookpark Road
Cleveland, OH 44135
Attention: Library

38 - 40 National Institute of Standards
and Technology
Gaithersburg, MD 20899
Attention: Metallurgy Division
Ceramic Division
Fracture and
Deformation Division

39 Naval Facilities Engineering
Command
Alexandria, VA 22331
Attention: Code 03

40 Commandant of the Marine Corps
Scientific Advisor
Washington, DC 20380
Attention: Code AX

41 Army Research Office
P. O. Box 12211
Research Triangle Park, NC 27709
Attention: Metallurgy & Ceramic Program

42 Army Materials Technology Laboratory
Watertown, MA 02172-0001
Attention: Research Program Office

43 Air Force Office of Scientific Research
Building 410, Bolling Air Force Base
Washington, DC 20332
Attention: Electronics & Materials
Science Directorate

44 NASA Headquarters
Washington, DC 20546
Attention: Code RM

45 Defense Metals & Ceramics Information
Center
Battelle Memorial Inst.
505 King Avenue
Columbus, OH 43201

46 Oak Ridge National Laboratory
Metals and Ceramics Division
P. O. Box X
Oak Ridge, TN 37380

47 Los Alamos Scientific Laboratory
P. O. Box 1663
Los Alamos, NM 87544
Attention: Report Librarian

48 Argonne National Laboratory
Metallurgy Division
P. O. Box 229
Lemont, IL 60439

49 Brookhaven National Laboratory
Technical Information Division
Upton, Long Island, NY 11973
Attention: Research Library

50 Lawrence Berkeley Laboratory
1 Cyclotron Road
Berkeley, CA 94720
Attention: Library

51 - 52 David Taylor Research Center
Annapolis, MD 21402-5067
Attention: Code 281
Code 2813
Code 0115

53 Profs. G. H. Meier & F. S. Pettit
Dept. of Metallurgical and Materials
Engineering
University of Pittsburgh
Pittsburgh, PA 15261

54 Prof. H. K. Birnbaum
Dept. of Metallurgy and Mining
Engineering
University of Illinois
Urbana, IL 61801

55 Prof. H. W. Pickering
Dept. of Materials Science and
Engineering
The Pennsylvania State University
University Park, PA 16802

56 Prof. D. J. Duquette
Dept. of Metallurgical Eng.
Rensselaer Polytechnic Inst.
Troy, NY 12181

57 Prof. D. Tomanek
Michigan State University
Dept. of Physics and Astronomy
East Lansing, MI 48824-1116

58 Dr. M. W. Kendig
Rockwell International Science
Center
1049 Camino Dos Rios
P. O. Box 1085
Thousand Oaks, CA 91360

59 Prof. R. A. Rapp
Dept. of Metallurgical Engineering
The Ohio State University
116 West 19th Avenue
Columbus, OH 43210-1179

60 Dr. R. D. Granata
Zettlemoyer Center for Surface
Studies, Sinclair Laboratory
Lehigh University
Bethlehem, PA 18015

61 Dr. G. D. Davis
Martin Marietta Laboratories
1450 South Rolling Road
Baltimore, MD 21227-3898

62 Dr. S. M. Lipka
Dept. of Ocean Engineering
Florida Atlantic University
Boca Raton, FL 33431-0991

63 Prof. J. Kruger
Dept. of Materials Science and Engineering
The Johns Hopkins University
Baltimore, MD 21218

64 Dr. B. G. Pound
SRI International
333 Ravenswood Avenue
Menlo Park, CA 94025

65 Prof. C. R. Clayton
Dept. of Materials Science and Engineering
State University of New York
Stony Brook
Long Island, NY 11794

66 Dr. J. W. Oldfield
Cortest Laboratories
23 Shepherd Street
Sheffield, S3 7BA, England

67 Prof. G. Simkovich
Dept. of Materials Science and Engineering
The Pennsylvania State University
University Park, PA 16802

68 Dr. R. V. Sara
Union Carbide Corporation
UCAR Carbon Company Inc.
Parma Technical Center
12900 Snow Road
Parma, OH 44130

69 Prof. M. E. Orazem
Dept. of Chemical Engineering
University of Florida
Gainesville, FL 32611

70 Prof. J. O'M Bockris
Dept. of Chemistry
Texas A & M University
College Station, TX 77843

71 Dr. V. S. Agarwala
Code 6062
Naval Air Development Center
Warminster, PA 18974-5000

72 Prof. Harovel G. Wheat
Dept. of Mechanical Engineering
The University of Texas
ETC 11 5.160
Austin, TX 78712-1063

73 Prof. S. C. Dexter
College of Marine Studies
University of Delaware
700 Pilottown Road
Lewes, DE 19958

74 Dr. Wayne C. Tucker
Dept. of Ocean Engineering
University of Rhode Island
Kingston, RI 02881

75 Mr. M. M. Opeka
Code K22
Naval Surface Warfare Center
Silver Spring, MD 20903-5000

76 Dr. E. McCafferty
Code 6322
Naval Researh Laboratory
Washington, DC 20375-5000

77 Dr. R. L. Jones
Naval Research Laboratory
Code 6179
Washington, DC 20375-5000

78 - 85 R. P. Gangloff

86 - 93 J. R. Scully

94 W. A. Jesser

* SEAS Postaward Administration

95 SEAS Preaward Administration

*Cover Letter
JO#4692:ph